# Sensitivity of cirrus bidirectional reflectance to vertical inhomogeneity of ice crystal habits and size distributions for two Moderate-Resolution Imaging Spectroradiometer (MODIS) bands

Ping Yang,[1,2] Bo-Cai Gao,[3] Bryan A. Baum,[4] Warren J. Wiscombe,[2] Yong X. Hu,[4] Shaima L. Nasiri,[5] Peter F. Soulen,[2,6] Andrew J. Heymsfield,[7] Greg M. McFarquhar,[7] and Larry M. Miloshevich[7]

**Abstract.** A common assumption in satellite imager-based cirrus retrieval algorithms is that the radiative properties of a cirrus cloud may be represented by those associated with a specific ice crystal shape (or habit) and a single particle size distribution. However, observations of cirrus clouds have shown that the shapes and sizes of ice crystals may vary substantially with height within the clouds. In this study we investigate the sensitivity of the top-of-atmosphere bidirectional reflectances for two Moderate-Resolution Imaging Spectroradiometer (MODIS) bands centered at 0.65 $\mu$m and 2.11 $\mu$m to cirrus models composed of either a single homogeneous layer or three distinct, but contiguous, layers. First, we define the single- and three-layer cirrus cloud models with respect to ice crystal habit and size distributions on the basis of in situ replicator data acquired during the First International Satellite Cloud Climatology Project (ISCCP) Regional Experiment (FIRE-II), held in Kansas during the fall of 1991. Subsequently, fundamental light-scattering and radiative transfer theory is employed to determine the single-scattering and the bulk radiative properties of the cirrus cloud. For radiative transfer computations we present a discrete form of the adding/doubling principle that is computationally straightforward and efficient. For the 0.65 $\mu$m band, at which absorption by ice is negligible, there is little difference between the bidirectional reflectances calculated for the one- and three-layer cirrus models. This result suggests that the vertical inhomogeneity effect is relatively unimportant at 0.65 $\mu$m. At 2.11 $\mu$m the bidirectional reflectances computed for both optically thin ($\tau = 1$) and thick ($\tau = 10$) cirrus clouds show significant differences between the results for the one- and three-layer models. The reflectances computed for the three-layer cirrus model are substantially larger than those computed for the single-layer cirrus. Furthermore, our analysis shows that the cirrus reflectances at both the 0.65 and 2.11 $\mu$m bands are very sensitive to the optical properties of the small crystals that predominate in the top layer of the three-layer cirrus model. It is critical to define the most realistic geometric shape for the small "quasi-spherical" ice crystals in the top layer for obtaining reliable single-scattering parameters and bulk radiative properties of cirrus.

## 1. Introduction

Cirrus clouds located in the upper troposphere and lower stratosphere are important to the Earth's climate [*Liou*, 1986; *Stephens et al.*, 1990]. They reflect solar radiation, absorb the thermal emission from the ground and the lower atmosphere, and

emit infrared radiation to space. The Moderate Resolution Imaging Spectroradiometer (MODIS) [*King et al.*, 1992] on the recently launched Terra spacecraft will enhance the capability for monitoring cirrus clouds in comparison with previous generations of satellite instruments such as the advanced very high resolution radiometer (AVHRR). MODIS has a total of 36 bands for studies of land, ocean, and the atmosphere, including the 1.38 $\mu$m band for cirrus detection and correction [*Gao and Kaufman*, 1995], the 0.65, 1.66, and 2.11 $\mu$m bands for implementing cloud microphysical and optical property retrieval techniques [*King et al.*, 1997] (available at http://eospso.gsfc.nasa.gov/atbd/modistables.html), and the 8.5, 11, and 12 $\mu$m bands for applying infrared cloud property retrieval techniques [*Ackerman et al.*, 1990]. MODIS data will allow improved retrievals of cirrus optical and microphysical parameters such as optical thickness of cirrus and mean effective size of the ice crystals in these clouds.

Various algorithms have been developed to retrieve cirrus optical and microphysical properties in the past 20 years [e.g., *Liou et al.*, 1990; *Ou at al.*, 1993; *Minnis et al.*, 1993a, 1993b; *Rossow and Lacis*, 1990]. They can be categorized into the

---

[1]Goddard Earth Science and Technology Center, University of Maryland Baltimore County, Baltimore, Maryland
[2]NASA Goddard Space Fight Center, Greenbelt, Maryland
[3]Remote Sensing Division, Naval Research Laboratory, Washington, D C
[4]NASA Langley Research Center, Hampton, Virginia
[5]Cooperative Institute for Meteorological Satellite Studies/University of Wisconsin, Madison, Wisconsin
[6]Joint Center for Earth Systems Technology, University of Maryland Baltimore County, Baltimore, Maryland
[7]National Center for Atmospheric Research, Boulder, Colorado

techniques based on either infrared emission or solar reflection. The representative algorithm of the former is the method developed by *Inoue* [1985] for determining the infrared emissivity of cirrus clouds on the basis of the brightness temperature difference between 11 μm and 12 μm wavelengths with an assumption of implicit mean particle size. An infrared trispectral algorithm using the 8.5, 11, and 12 μm bands [*Ackerman et al.*, 1990, 1998; *Strabala et al.*, 1994] with a recent improvement [*Baum et al.*, 2000a, 2000b] forms the basis of an infrared retrieval algorithm using MODIS infrared channels. The representative retrieval algorithm based on solar reflection is that developed by *Nakajima and King* [1990], who used a trispectral (0.75, 1.6, and 2.2 μm) method to simultaneously retrieve the optical thickness and mean effective particle size for water clouds. This approach has been applied to the retrieval of the optical thickness and mean particle size of ice crystals for cirrus [*Wielicki et al.*, 1990].

To develop a reliable retrieval algorithm for cirrus optical and microphysical properties, it is critical to generate reliable precalculated lookup tables of bidirectional reflectance for cirrus clouds over a practical range of effective sizes, optical thicknesses, and viewing geometry (i.e., solar zenith angle, viewing zenith angle, and relative azimuth angle). At present, most algorithms for retrieving cirrus optical thickness and effective size assume that the ice crystals are of one specific habit, such as spheres, hexagonal plates, hexagonal columns, or fractal polycrystals [*Macke et al.*, 1996]. In addition, a common assumption is that a single size distribution is sufficient to determine the scattering properties of the ice crystals within the cirrus layer. However, observations based on aircraft-borne two-dimensional optical cloud probe (2D-C) and balloon-borne replicator measurements [e.g., *Heymsfield and Platt*, 1984; *Arnott et al.*, 1994; *Mitchell et al.*, 1996a, 1996b; *McFarquhar and Heymsfield*, 1996, 1997] demonstrate the wide range of shapes that the ice crystals in cirrus clouds may have, including bullet rosettes, solid and hollow columns, plates, and irregularly shaped aggregates. In addition, Heymsfield and colleagues have showed that ice crystal habits and size distributions are vertically inhomogeneous in cirrus clouds [e.g., *Heymsfield and Iaquinta*, 2000].

Since satellite-based retrieval techniques essentially compare library computations of bidirectional reflectances to actual measurements in their implementations, it is necessary to assess the effect of the vertical inhomogeneity of the ice crystal sizes and shapes within cirrus on the radiative transfer calculations for generating the reflectance libraries. Our objective is to understand the effect of the vertical inhomogeneity in the structure of cirrus clouds on their radiative properties. We employ fundamental scattering and radiative transfer theory to investigate the bidirectional reflectance of cirrus clouds for the MODIS 0.65 and 2.11 μm bands using in situ crystal habit and size distribution for a case of midlatitude cirrus on November 25, 1991, further described in section 2.

The outline of the paper is as follows. The data and models are provided in section 2. Section 3 describes the development of the three-layer and single homogeneous cirrus models as well as the single-scattering properties associated with the two cirrus models. In section 4 we present the differences between bidirectional reflectances computed for the three-layer cirrus model and its one-layer counterpart. Also presented in this section is a sensitivity study regarding the shape effect of the small "quasi-spherically" nonspherical ice crystals on cloud reflectance. Conclusions are given in section 5. Finally, in Appendix A we

present a numerically stable radiative transfer model based on the adding/doubling principle. The adding/doubling model is expressed in a discrete form for calculating reflected and transmitted intensities resulting from multiple scattering and absorption of cirrus clouds.

## 2. Data and Models

### 2.1. Data

The size distributions and ice crystal habit information obtained from two cases of replicator measurements carried out in Kansas during the First International Satellite Cloud Climatology Project (ISCCP) Regional Experiment (FIRE) [*Starr*, 1987] phase II (hereafter, FIRE-II) are used in this study. The balloon-borne ice crystal replicators were launched at 1337 UTC on November 25, 1991, and at 2045 UTC on December 5, 1991. The replicator balloons had an ascent rate of approximately 4 m s$^{-1}$ while passing through the cloud layers. As measured by a radiosonde connected to the balloon package, the cloud top temperature on November 25 was −57°C, while on December 5 the cloud top temperature was −65°C.

The replicator collects particles in a liquid plastic solution that coats a moving, 35-mm-wide transparent leader tape. The particles become imbedded in the plastic coating, and when the solvent in the solution evaporates, detailed ice crystal impressions and size spectra of crystals are recorded down to crystal sizes of approximately 10 μm. The particles generally do not break up upon impact on the replicator tape because of the slow rate of ascent of the balloon. The efficiency with which the replicator collects small crystals has been quantified theoretically and experimentally [*Miloshevich* and *Heymsfield*, 1997]. Particle size concentrations used in this study are adjusted to account for the imperfect collection efficiencies of small particles. Analysis of the ice crystal data collected during the balloon's ascent through the cirrus provided 28 size spectra in the vertical on November 25 and 33 spectra on December 5, with each spectrum representing the data collected from approximately 100 m of vertical ascent.

### 2.2 Single-Scattering Properties

The range of ice crystal sizes in cirrus clouds is predominately within the applicable size parameter regime of the geometric optics method at visible and near-infrared wavelengths. Each ray can be localized on the wave front of the incident radiation (electromagnetic wave); consequently, Snell's law and Fresnel's formulas can be applied to trace the ray propagation and the electric field magnitude, as well as the polarization configuration associated with the ray. In the conventional geometric optics approach for deriving the scattering properties of a particle, the scattered field in the radiation zone is regarded as the superposition of diffracted rays and Fresnelian rays. The contribution from ray diffraction can be determined using the standard Fraunhofer theory, whereas the contribution from Fresnelian rays can be computed by the ray-tracing technique. This approach suffers from several shortcomings, as was noted by *Yang and Liou* [1995]. In particular, it is assumed that the extinction efficiency is 2 regardless of particle size.

To overcome the shortcomings of the conventional geometric optics, *Yang and Liou* [1996] developed a geometric-optics-integral-equation approach (hereafter referred to as GOM2). According to fundamental electrodynamics theory, the scattered far field can be obtained if the tangential components of the

electric and magnetic fields on the particle surface are specified. In principle, GOM2 employs the ray-tracing technique to solve the near field on the particle surface and then maps the near field to the far field via the following rigorous electromagnetic relationship:

$$E^s(r)\big|_{kr\to\infty} = \frac{e^{ikr}}{-ikr}\frac{k^2}{4\pi}\hat{r}\times \oiint_S \{\hat{n}_s\times E(r')$$

$$- \hat{r}\times[\hat{n}_s\times H(r')]\}e^{-ik\hat{r}\cdot r'}d^2r', \qquad (1)$$

where $\hat{n}_s$ and $\hat{r}$ are unit vectors along the normal directions of particle faces and scattering direction, respectively, and $k = 2\pi/\lambda$ in which $\lambda$ is the wavelength of an incident wave in a vacuum. With GOM2 it is not necessary to partition the diffraction and Fresnelian contributions to the far field. A simplified algorithm for GOM2 is employed to reduce the computational cost.

To compute the extinction and absorption cross sections of ice crystals, we use the ray-tracing technique coupled with the following exact electrodynamic relationships:

$$C_{ext} = \text{Im}\left\{\frac{k}{|E_o|^2}\iiint_V[\varepsilon(r')-1]E(r')\cdot E_o^*(r')d^3r'\right\}, \qquad (2a)$$

$$C_{abs} = \frac{k}{|E_o|^2}\iiint_V \varepsilon_i(r')E(r')\cdot E^*(r')d^3r', \qquad (2b)$$

where $C_{ext}$ and $C_{abs}$ are extinction and absorption cross sections, respectively, $E_o$ is the electric field associated with the incident wave, $\varepsilon = \varepsilon_r + i\varepsilon_i$ is the complex permittivity, and the asterisk indicates the complex conjugate operation. The volume integrals in equations (2a) and (2b) are carried out along individual ray paths inside the particle via a Monte Carlo/ray-by-ray algorithm [Yang and Liou, 1997] that is a generalization of the well-known anomalous diffraction theory [van de Hulst, 1957].

Because of the complicated mechanisms involved in ice crystal growth, such as sublimation, riming, or the aggregation of particles, the surfaces of ice crystals may be rough. Roughened ice crystal surfaces have been observed in laboratory experiments [Cross, 1968] and in recent in situ observations of tropic anvil cirrus clouds (A. J. Heymsfield, private communication, 1999). The scattering phase functions of roughened particles display less variation [Macke et al., 1996; Yang and Liou, 1998] than their counterparts for ice crystals possessing smooth facets. As articulated by Mishchenko et al. [1996] on the basis of ground-based nephelometer and aircraft radiance measurement of cirrus clouds [Foot, 1988; Francis, 1995; Gayet et al., 1995; Posse and von Hoyningen-Huene, 1995], the scattering phase functions for some ice phase clouds can be rather featureless with no appreciable halos.

Based on these studies, we account for surface roughness specifically for ice crystal aggregates in this study. In the numerical computation the particle surface is regarded as a number of small facets whose normal direction is tilted from that in the smooth case, specified by local zenith and azimuth angles $\theta$ and $\varphi$, respectively. The slope of a facet along two orthogonal directions that are perpendicular to the local zenith direction, say, the $x$ and $y$ directions, can be specified by

$$Z_x = \frac{\partial Z}{\partial x} = (\mu^{-2}-1)^{1/2}\cos\varphi, \qquad (3a)$$

$$Z_y = \frac{\partial Z}{\partial y} = (\mu^{-2}-1)^{1/2}\sin\varphi, \qquad (3b)$$

where $\mu = \cos\theta$. The derivatives in equations (3a) and (3b) are confined to the facet. The geometric configuration associated with these two equations has been illustrated by Cox and Munk [1954]. Since there is little quantitative experimental information regarding the roughness of ice crystal surfaces at present, the surface roughness is treated in a similar fashion to that of a wavy sea surface, which can be specified by the Gram-Charlie distribution [Cox and Munk, 1954]. If the tilt distribution of the roughness is azimuthally homogeneous (i.e., independent of angle $\varphi$), the statistical probability density function for the condition that the slopes of a facet along the two axis directions are given by the first-order Gram-Charlie, or a two-dimensional (2-D) Gaussian distribution, is as follows:

$$P(Z_x, Z_y) = \frac{1}{\pi\sigma^2}\exp[-(Z_x^2 + Z_y^2)/\sigma^2], \qquad (4)$$

where $\sigma$ is a parameter determining the magnitude of roughness. Values of $\sigma = $ 0-0.005, 0.005-0.05, 0.05-0.3 correspond to slight, moderate, and deep roughness in the single-scattering calculation, respectively. Further technical details concerning the treatment of surface roughness in the GOM2 light scattering computations were given by Yang and Liou [1998].

### 2.3. Radiative Transfer Model

Radiative transfer calculations for cirrus are performed using the adding/doubling method. The adding/doubling principle has been expressed mathematically in a matrix form [Twomey, 1966; Hunt and Grant, 1966] and in an integral form [Hansen and Travis, 1974]. A concise formulation in a discrete form for the adding/doubling method is provided in Appendix A. In Appendix A, some numerical concerns in the radiative transfer computation are addressed, such as the truncation of the forward scattering peak in the phase function and a stable expansion of the phase function in terms of the renormalized Legendre function. The discrete expression of the adding/doubling principle is straightforward and efficient in numerical realization. The present adding/doubling computational program has been validated with respect to the various cases presented by Lenoble [1985] and also in comparison with the discrete ordinate method radiative transfer model (DISORT) [Stamnes et al., 1988] (also ftp://climate.gsfc.nasa.gov/pub/wiscombe/Multiple_Scatt/DISORT_1.2/DISORTReport.pdf) for a number of canonical problems.

## 3. Development of Cirrus Models

### 3.1. Cirrus Three-Layer Model

The vertically inhomogenous nature of cirrus clouds was observed during the FIRE-II program. Figures 1a and 1b show two different vertical profiles based on replicator images of ice crystals in cirrus clouds collected on November 25 and December 5, 1991. For these two cases, three distinct regimes of ice crystals are evident from the replicator data. In the uppermost layer, small nonspherical "quasi-spheres" are predominant. The middle layer of cirrus is composed primarily of pristine ice crystals with well-defined hexagonal shapes or bullet rosettes. The bottom layer contains larger but irregular aggregates. The edges of these irregular ice crystals seem to be rounded, perhaps due to the effect of sublimation. Roughness can also be noted from the replicator images of the irregular ice crystals. In t3th images it is apparent that the particles increase in size and the shapes become more complex from the top to the base of the cirrus.
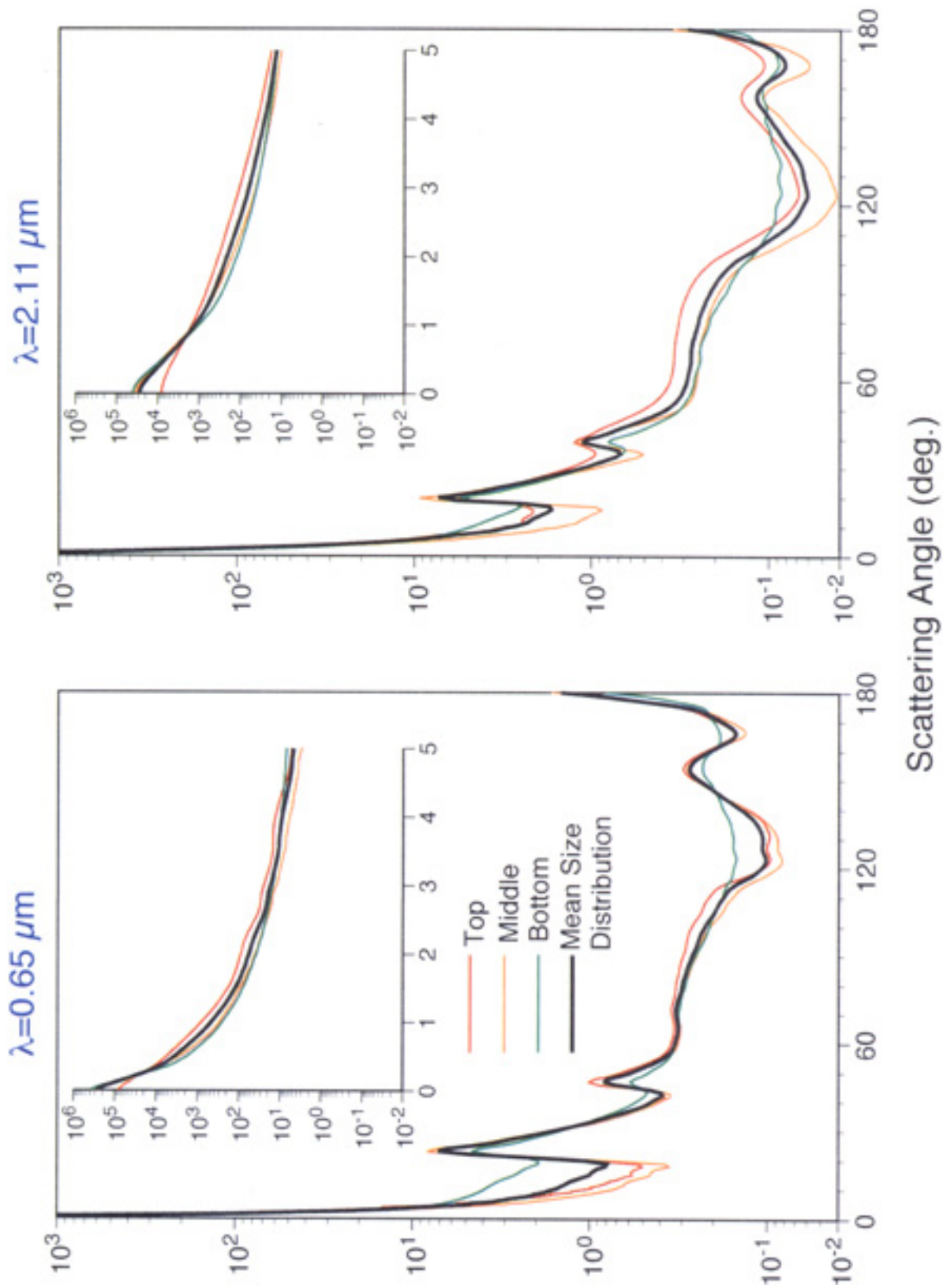
**Plate 1.** Phase function corresponding to the single-scattering properties shown in Figure 3b.
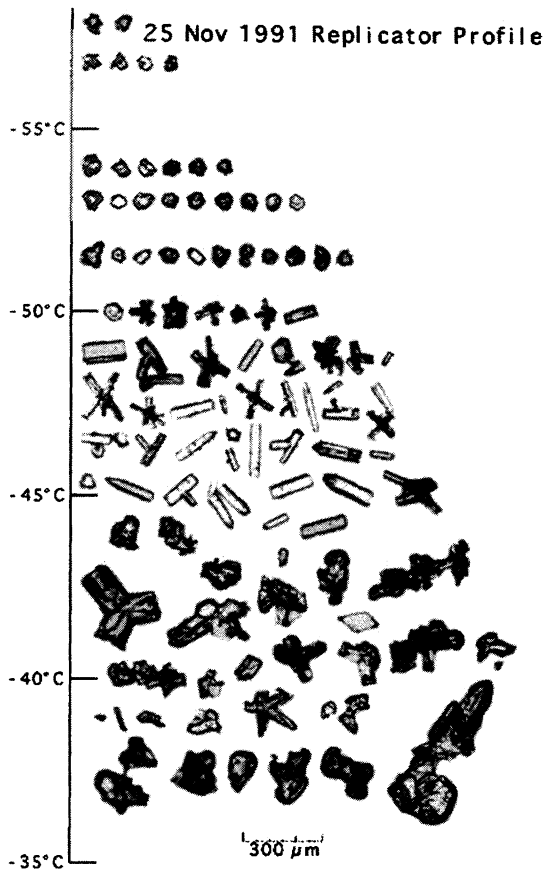
**Figure 1a.** Replicator images of ice crystals from a cirrus cloud observed on November 25 1991 during the First International Satellite Cloud Climatology Project (ISCCP) Regional Experiment (FIRE-II) field experiment [after *Heymsfield and Iaquinta*, 2000 with permission of the American Meteorological Society]. Note the three-layer structure with small quasi-spherical crystals in the top layer, and columns and bullet rosettes in the second layer. The third layer is composed mostly of large aggregated crystals.

The small particles in the uppermost layer have nonspherical shapes with an aspect ratio approaching 1. Sometimes the term "quasi-spherical" is used in the analysis of observed data and in theoretical studies. This term is often misleading because the optical properties of spherical and nonspherical particles are significantly different even if the nonsphericity of particle geometry is not substantial.

Analysis of the replicator data has yielded detailed information on the dominant habits of ice crystals and size distributions for the two cases shown in Figures 1a and 1b. As discussed in section 2.1, data were obtained for 28 and 33 vertical layers at approximately 100 m resolution in FIRE-II in situ observations for the November 25 and December 5 cases, respectively. Using these data, we constructed the percentages of the various ice crystal habits and size distributions for the top, middle, and bottom layers of cirrus clouds. For a given layer centered at $z$ with thickness of $\Delta z$, the mean size distribution and percentage of a specific habit are given by

$$\bar{n}(D,z) = \frac{1}{\Delta z} \int_{z-\Delta z/2}^{z+\Delta z/2} n(D,z') \, dz', \qquad (5a)$$

$$\bar{f}_i(D,z) = \frac{\int_{z-\Delta z/2}^{z+\Delta z/2} f_i(D,z') n(D,z') \, dz'}{\int_{z-\Delta z/2}^{z+\Delta z/2} n(D,z') \, dz'}, \qquad (5b)$$

where $D$ is the maximum dimension of ice crystals. The preceding averaging procedure is also applied to obtain the mean size distribution and habit percentage for cirrus by assuming a single size distribution to represent the cirrus cloud.

To illustrate the differences between the use of a three-layer model and a single-layer cirrus model, we first confine our discussion to the November 25 case where the cirrus cloud spanned a vertical range of 2.7 km and had a total optical thickness of approximately 1. The geometric heights of the top, middle, and bottom layers are 0.79, 0.73, and 1.18 km, respectively. The size distributions and crystal habit percentages for the three layers are shown in histograms A, B, and C of Figure 2a. For the uppermost cirrus layer, "quasi-spherical" habits are dominant for the small-particle mode ($D < 100$ μm), whereas bullet rosettes are dominant for the large-particle mode ($D > 100$ μm). The middle layer is composed primarily of columns and bullet rosettes. In the bottom layer, ice crystals are mainly irregular aggregates. The percentages of various ice crystal habits integrated over the entire cirrus layer are shown in histogram D of Figure 2a. Two geometries (sphere and hexagon) are used to represent the small ice crystals, as is illustrated in histograms A and D of Figure 2a. The two particle morphologies are chosen to investigate the sensitivity of the radiative properties of cirrus to the presence of these small ice crystals near cloud top.
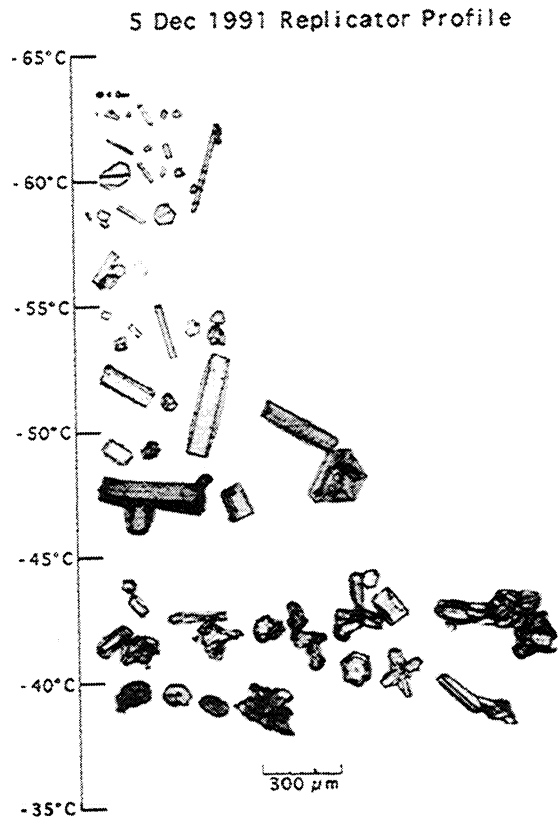


**Figure 1b.** Same as Figure 1a, except that the observation was made on December 5, 1991, and the top layer is dominated by pristine columns. Data courtesy of L. Miloshevich and S. Aulenbach, National Center for Atmospheric Research.
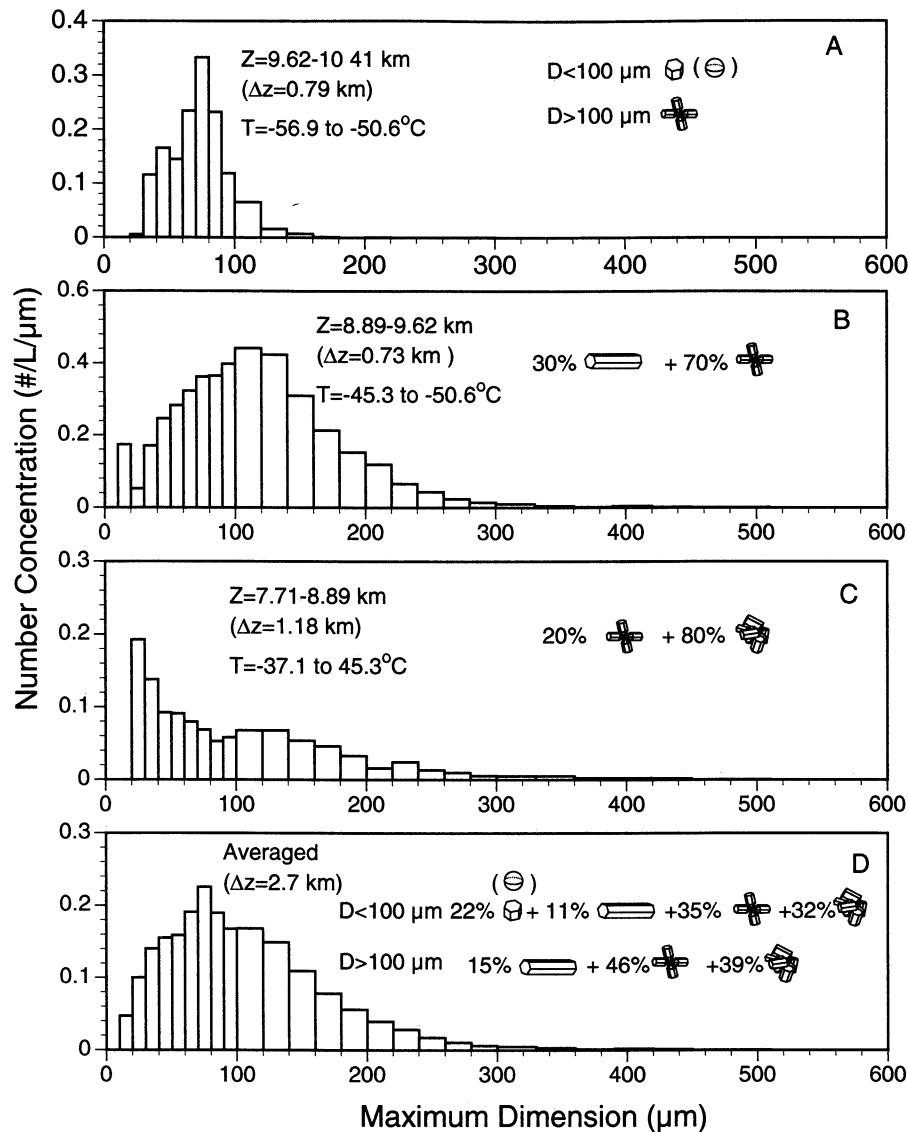
Z=9.62-10 41 km
(Δz=0.79 km)
T=-56.9 to -50.6°C

D<100 μm

D>100 μm

A

Z=8.89-9.62 km
(Δz=0.73 km )
T=-45.3 to -50.6°C

30%  + 70%

B

Z=7.71-8.89 km
(Δz=1.18 km)
T=-37.1 to 45.3°C

20%  + 80%

C

Averaged
(Δz=2.7 km)

D<100 μm 22% + 11%  +35%  +32%

D>100 μm  15%  + 46%  +39%

D

Number Concentration (#/L/μm)

Maximum Dimension (μm)

**Figure 2a.** Size distribution modeling the cirrus observed on November 25, 1991, that is shown in Figure 1a. Histograms A, B, and C show the size and habit distributions for the top, middle, and bottom layer, respectively. Histograms D shows the mean size distribution averaged over height.

These small ice crystals are often misidentified as spheres in observations based on the particle images with blurred edges. Even with the use of an optical microscope, the shapes of small ice crystals are unlikely to be seen clearly because of the poor instrumental resolving power caused by optical diffraction phenomena [*Ohtake*, 1970].

Shown in Figure 2b are the size distributions and habit percentages for the case of December 5. The geometric heights of the three layers are 1.24, 1.12, and 1.17 km, respectively. The December 5 case had a colder cloud top temperature than for the November 25 case, and many hexagonal columns and small "quasi-spherical" droxtals [*Thuman and Robinson*, 1954; *Ohtake*, 1970] were observed in the crystal population. The division of large and small modes for ice crystal habits is at 50 μm for the case of December 5. Again, "quasi-spherical" ice crystals seem to dominate the small-particle mode. There are substantially large numbers of "quasi-spherical" particles even for the middle layer.

According to Figures 2a and 2b, both size distributions and ice crystal habits vary substantially with altitude. While insufficient evidence exists to make generalizations regarding the vertical size distribution of ice particles in cirrus clouds, there are additional analyses in this regard based on radar observations [*Mace et al.*, 1997] that tend to support the concept of multiple-layered cirrus clouds with composite morphologies.

### 3.2. Radiative Properties of Cirrus Layers

We employ the scattering computational model described in section 2 to compute the extinction cross sections, single-scattering albedos, and phase functions for ice crystals. Ice crystals are assumed to be orientated randomly in the atmosphere. First, to characterize the bulk properties of size distribution, 6/e define the mean maximum dimension for a given size distribution as follows:
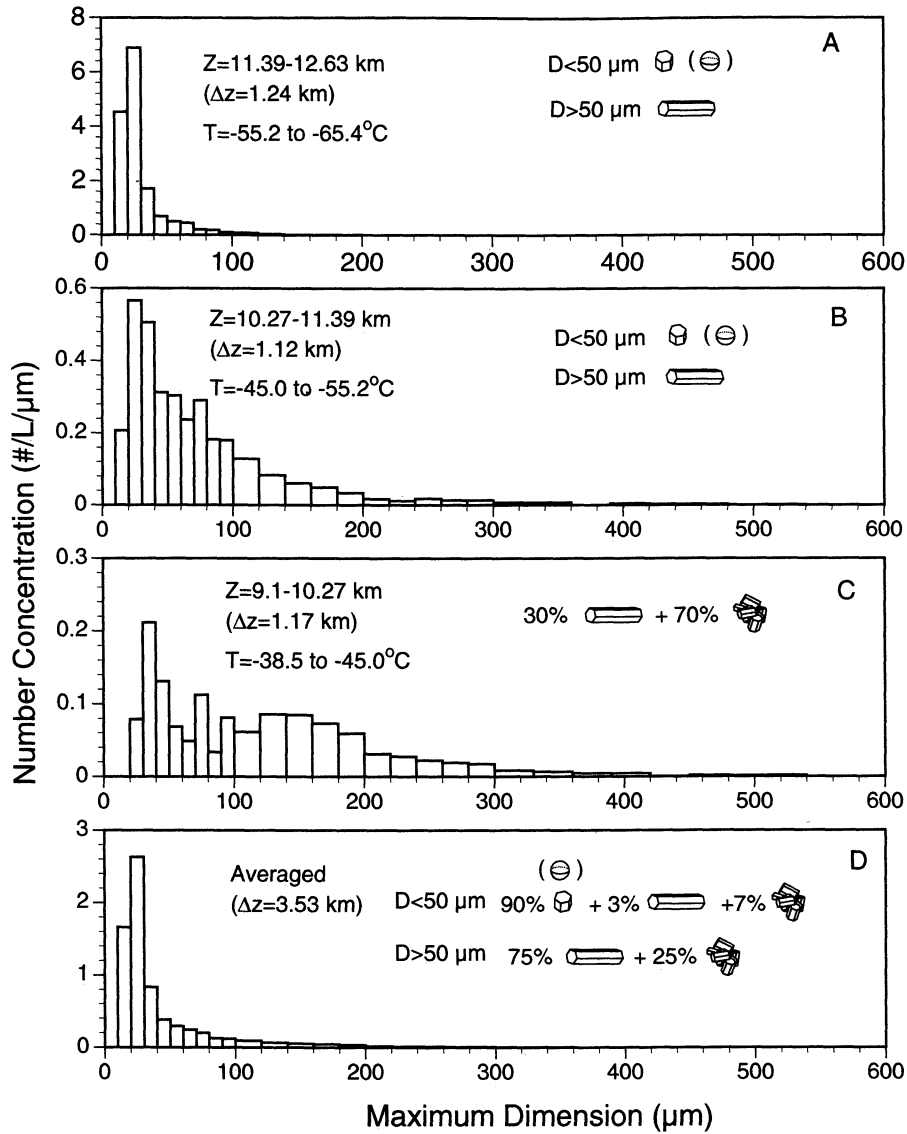
**Figure 2b.** Same as Figure 2a except for the case of December 5, 1991.

$$< D > = \frac{\int_{D_{min}}^{D_{max}} D n(D) dD}{\int_{D_{min}}^{D_{max}} n(D) dD}, \quad (6)$$

where $D_{min}$ and $D_{max}$ are the cutoffs of size distribution at small and large sizes, respectively. Studies by *Foot* [1988], *Francis et al.* [1994], *Fu* [1996], and *Wyser and Yang* [1998] have found that the details of the size distribution are not important to specifying the bulk optical properties of cirrus with respect to the effective size of ice crystals if the effective size is defined as the ratio of total volume to the total projected area. This feature has also been observed in the case of water clouds composed of liquid droplets whose scattering properties can be solved using Mie theory [*Hansen and Travis*, 1974; *Hu and Stamnes*, 1993]. Following these studies, we define the effective diameter $D_e$ and effective radius $r_e$ for nonspherical ice crystals with a combination of various habits as follows:

$$D_e = 2r_e = \frac{3}{2} \frac{\int_{D_{min}}^{D_{max}} \sum_i V_i(D) f_i(D) n(D) dD}{\int_{D_{min}}^{D_{max}} \sum_i A_i(D) f_i(D) n(D) dD}, \quad (7)$$

where $f_i(D)$ is the percentage of a specific habit at size $D$. The summation over index $i$ is carried out for all the ice crystal habits. We note that the preceding definition of effective radius reduces to that defined by *Hansen and Travis* [1974] in the case of spherical particles, that is, $r_e = < r^3 > / < r^2 >$. The mean extinction cross section, single-scattering albedo, and phase function are given by

$$\overline{C}_{ext} = \frac{\int_{D_{min}}^{D_{max}} \sum_i C_{ext,i}(D) f_i(D) n(D) dD}{\int_{D_{min}}^{D_{max}} \sum_i f_i(D) n(D) dD}, \quad (8a)$$

$$\tilde{\omega} = \frac{\int_{D_{min}}^{D_{max}} \sum_i C_{scat,i}(D) f_i(D) n(D) dD}{\int_{D_{min}}^{D_{max}} \sum_i C_{ext,i}(D) f_i(D) n(D) dD}, \quad (8b)$$

$$\overline{P}(\Theta) = \frac{\int_{D_{min}}^{D_{max}} \sum_i C_{scat,i}(D) P_i(\Theta,D) f_i(D) n(D) dD}{\int_{D_{min}}^{D_{max}} \sum_i C_{scat,i}(D) f_i(D) n(D) dD}, \quad (8c)$$
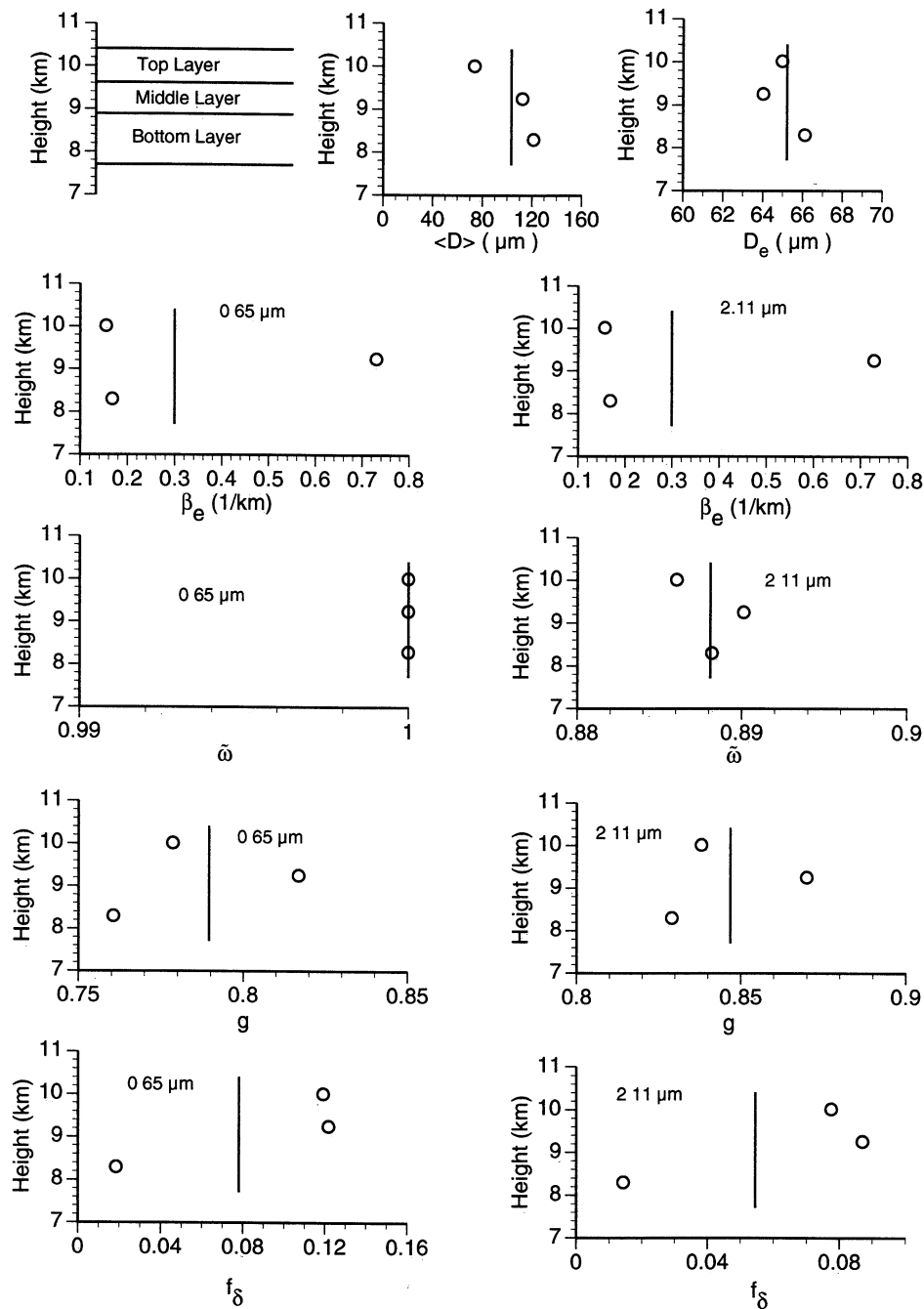
7

**Figure 3a.** The mean size and single-scattering properties for the three-layer (November 25, FIRE-II) cirrus model. The vertical lines indicate the results computed using the one-layer model mean size distribution (i.e., the cloud is assumed to be vertically homogeneous).

where $C_{scat,i}$ is the scattering cross section of habit $i$, given by the difference of extinction and absorption cross sections that can be computed on the basis of equations (2a) and (2b).

Figures 3a and 3b show the bulk microphysical and optical properties for the size distributions shown in Figures 2a and 2b. The upper row shows the geometric configuration of the three layers of cirrus and the mean maximum dimension and effective size of ice crystals in these layers. The second and third rows show the extinction coefficient and single-scattering albedo. Note that the extinction coefficient associated with a specific cirrus layer is given by the mean extinction cross section and the

thickness of the layer. The lower two rows provide the asymmetry parameter of the phase functions and the fraction of delta transmission [*Takano and Liou*, 1989a] in scattered energy. Note that the delta transmission is an artifact pertaining to the ray-tracing technique, which can be circumvented by using a more accurate physical optics approach [*Mishchenko and Macke*, 1998]. In the present GOM2 calculation based on a simplified algorithm [*Yang and Liou*, 1996], we do not account for the spreading of the rays associated with delta transmission for size parameters larger than 100. The use of either a geometric optics method or a physical optics approach in dealing with delta

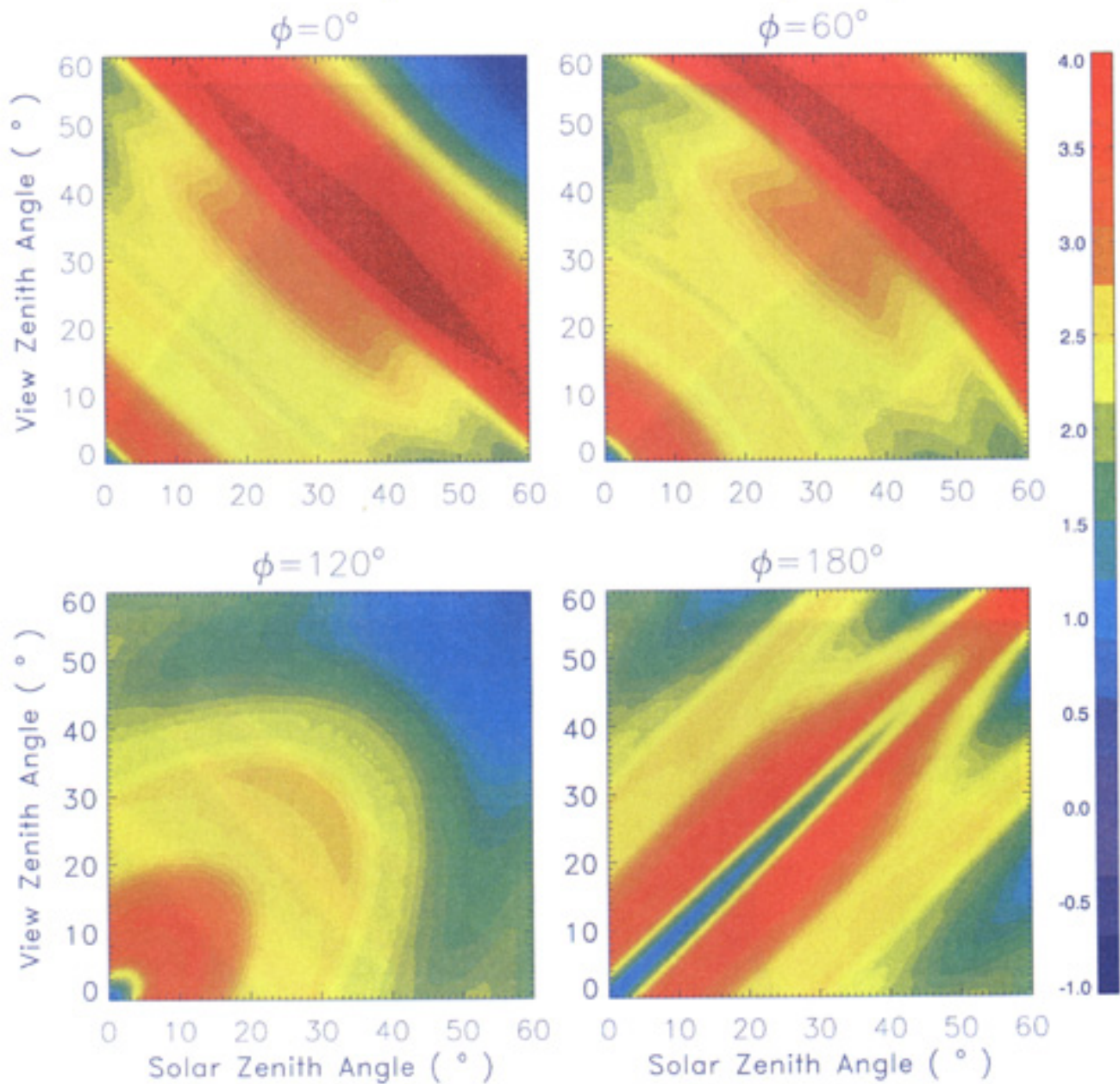# $\lambda=0.65\ \mu\mathrm{m}$, Thin Cirrus $(\tau=1)$



**Plate 2.** The percent relative difference of bidirectional reflectance computed using the three- and one-layer models at MODIS 0.65 μm band for thin cirrus (τ=1). The maximum difference for this case is about 5% and depends mainly on scattering angle.
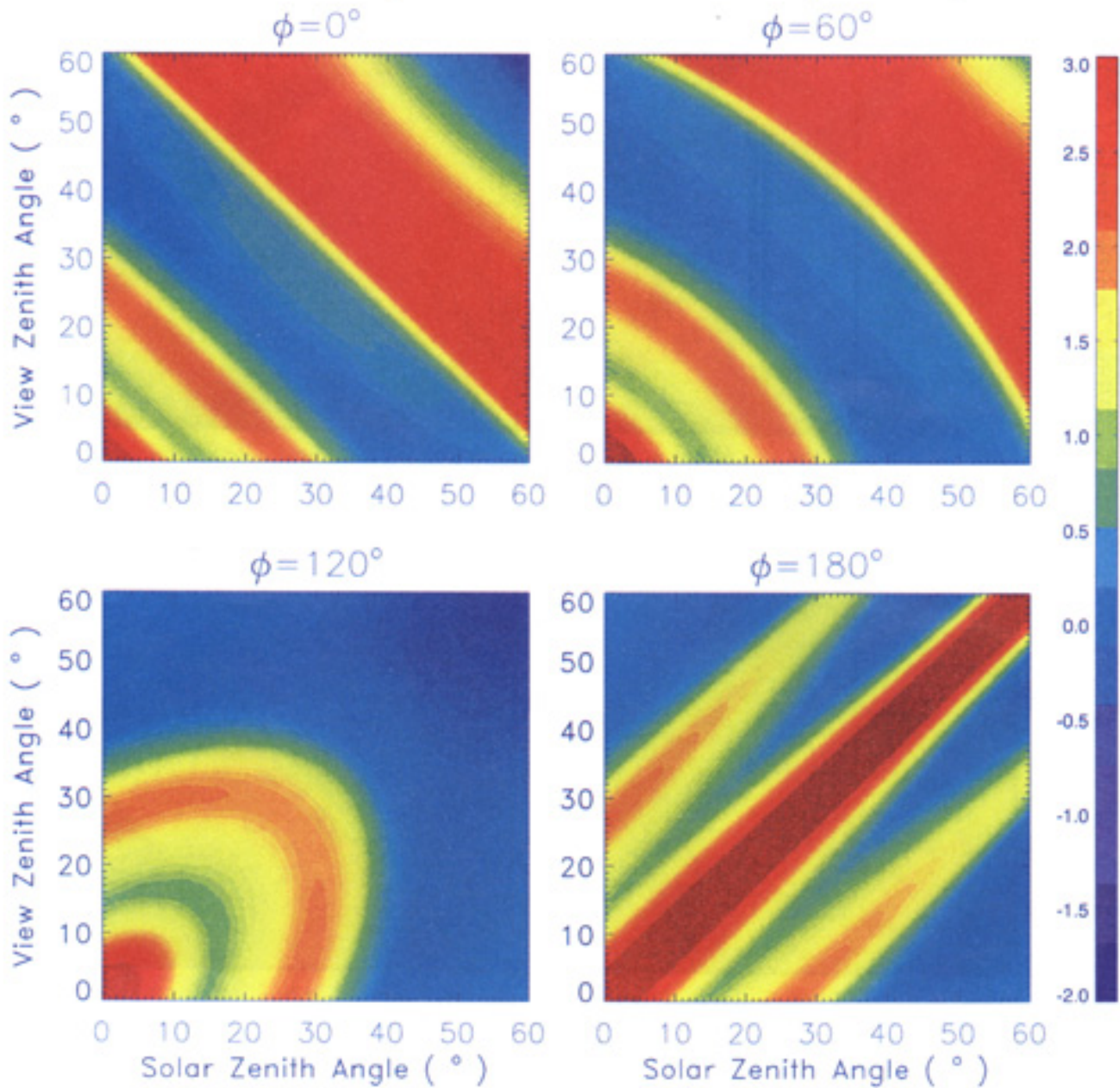
**Plate 3.** Same as Plate 2, except for thick cirrus ($\tau$=10).
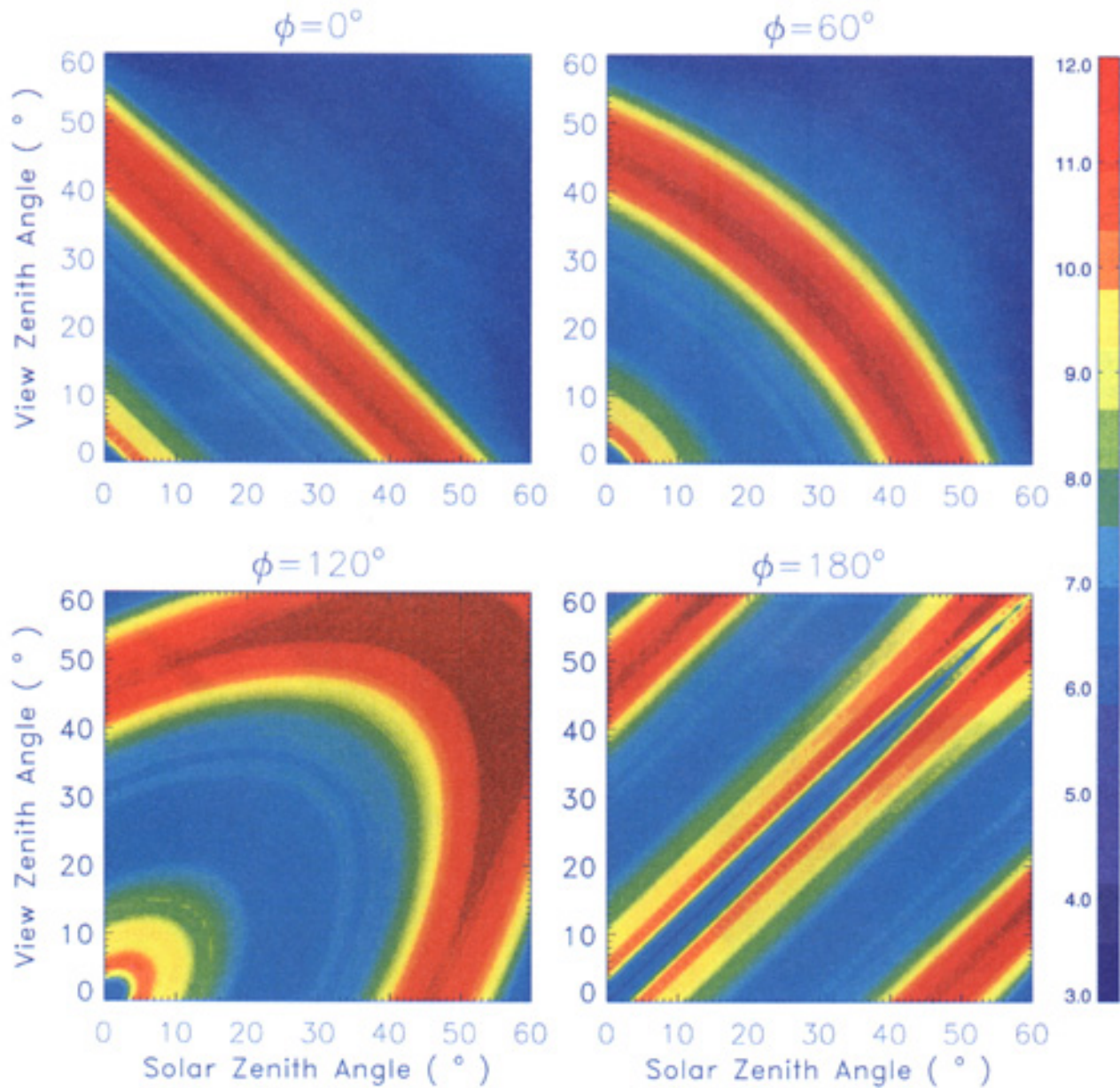
# $\lambda=2.11\ \mu m$, Thin Cirrus $(\tau=1)$



**Plate 4.** Same as Plate 2, except for MODIS 2.11 μm band. Note the relative difference is much higher (up to 12%) than at 0.65 μm wavelength due to absorption by ice.
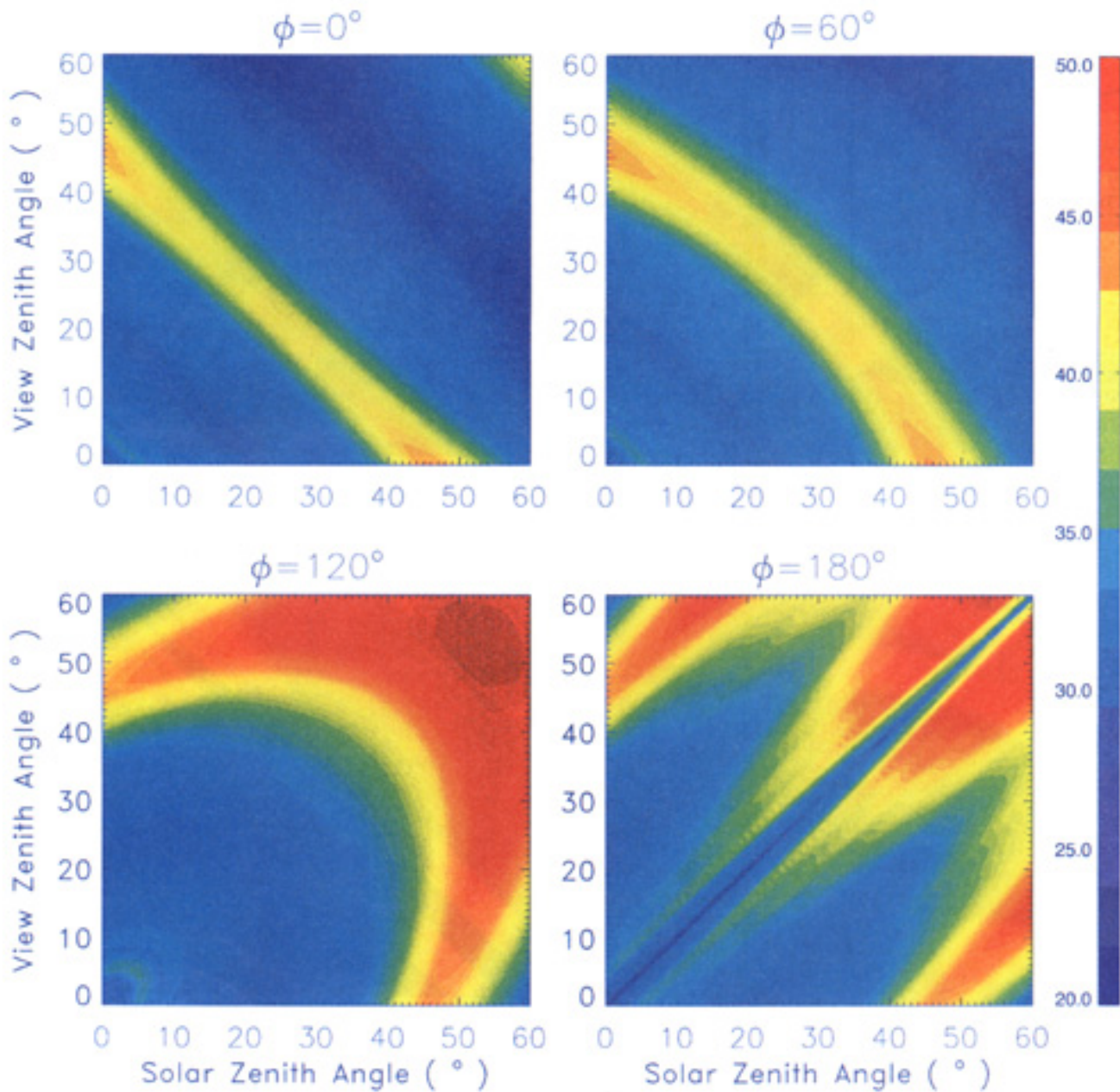
**Plate 5.** Same as Plate 3, except for MODIS 2.11 μm band.  The differences for large optical thickness reach up to 50% and depend also on viewing and solar zenith angles.
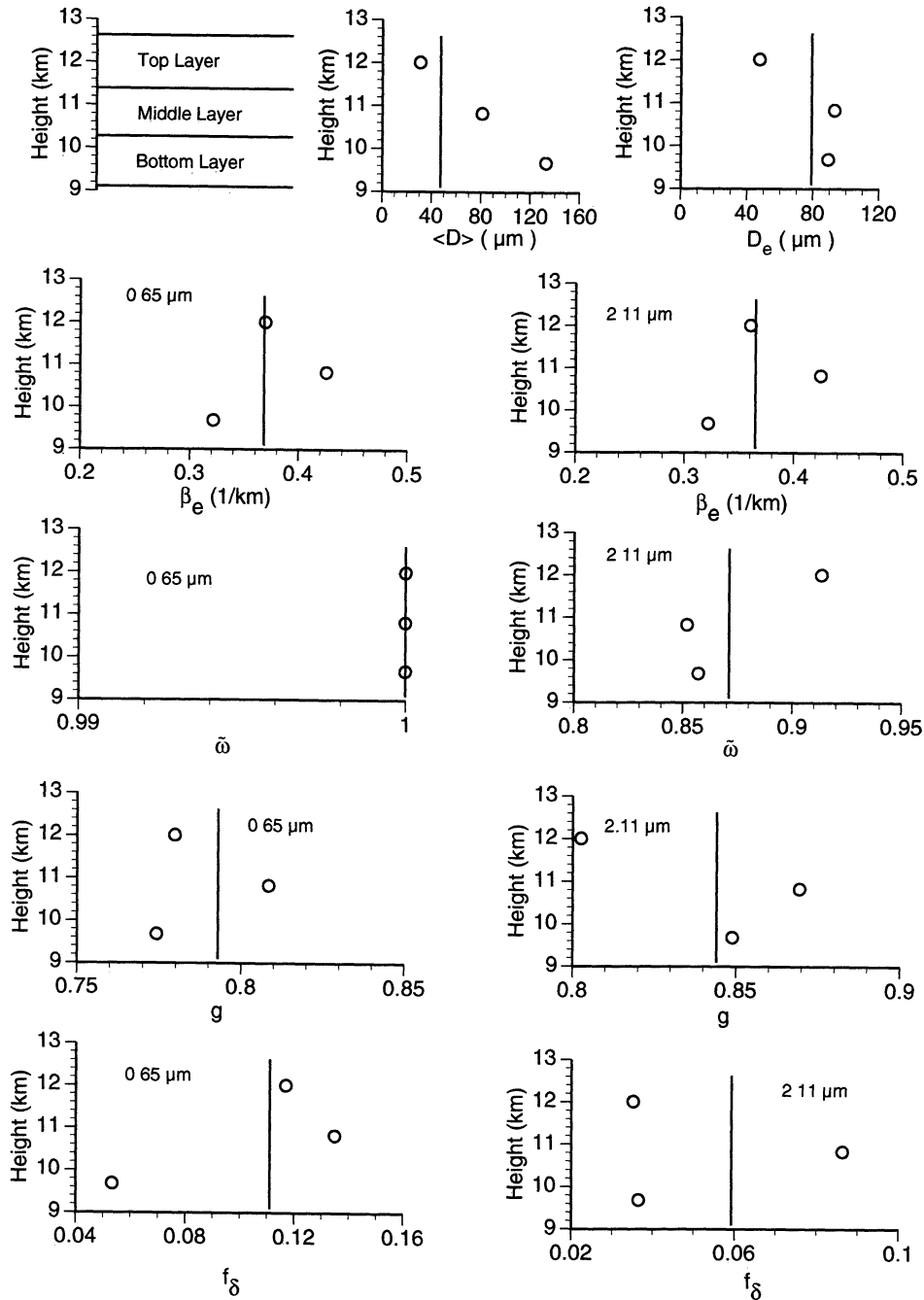
**Figure 3b.** Same as Figure 3a, except for the December 5 case that is shown in Figure 2b.

transmission in the single-scattering calculation for large size parameters does not make a significant difference in the radiative transfer computation.

For the November 25 case (Figure 3a), the mean maximum dimension of the ice crystals is 74 μm, 112 μm, and 121 μm for the top, middle, and bottom cirrus layers. The mean effective diameters for the top, middle, and bottom cirrus layers are 65, 64, and 66 μm, respectively. For the December 5 case (Figure 3b), the mean maximum dimension of the ice crystals is 30 μm, 80 μm, and 132 μm for the top, middle, and bottom cirrus layers, respectively. The corresponding mean effective diameters are 47, 92, and 89 μm for the top, middle, and bottom layers, respectively. We note that the effective diameters for the middle

and bottom layers are substantially smaller for the November 25 case than for the December 5 case. The reason for this is that there are high numbers of bullet rosettes in the November 25 case, and bullet rosettes tend to have a small ratio of volume to projected area. In addition, the smaller mean effective diameter may be attributed in part to the porous structures of ice crystal aggregates which are present in a larger number concentration on November 25 than on December 5.

The optical properties of ice crystals are computed for wavelengths representative of two MODIS bands centered at 13.5 and 2.11 μm. These wavelengths were chosen to represent the MODIS bands by integrating over the instrumental response functions following *Baum et al.* [2000a]. For the 0.65 and

2.11 μm bands, the maximum extinction coefficient is derived for the middle layer for both the November 25 and December 5 cases. This occurs because the number concentration of ice crystals is substantially higher in the middle layer than in the bottom layer. The number concentration in the top layer may not be lower than in the middle layer, but the cross sections for the small ice particles in the top layer are very small in comparison with those of the particles in the middle layer.

In the November 25 case, the single-scattering albedo at 2.11 μm for the middle layer is larger than the ones associated with the top and bottom layers because of the small effective particle size of the middle layer. Since the effective size is defined as the ratio of volume to projected area, which is proportional to the mean path length of rays inside the particles, a small effective size implies less absorption and thus a larger value of the single-scattering albedo. In contrast, the single-scattering albedo at 2.11 μm for the December 5 case is higher in the top layer than in the lower layers due to the prevalence of small crystals within the top layer.

For both bands the asymmetry parameter is smaller in the top and bottom layers than in the middle layer for both the November 25 and December 5 cases. In the top layer the asymmetry parameter is reduced because the particles are smaller, which tends to reduce the magnitude of the forward peak of the phase function. In the bottom layer the reduced asymmetry parameter is caused by the particle roughness.

The vertical variability of delta transmission is similar to that of the asymmetry parameter. In the top layer, delta transmission is substantially reduced in the December 5 case because of the ray-spreading effect associated with small size parameters [*Yang and Liou*, 1996]. In the bottom layer the roughness of particle surface also reduces the delta transmission effect. For the sake of brevity of presentation, in the following discussions we select the December 5 case to investigate the effect of vertical inhomogeneity on phase function and multiple-scattering properties of cirrus.

Plate 1 shows the phase functions associated with the single-scattering properties shown in Figure 3b. At 0.65 μm, substantial differences between the phase functions for the bottom layer and other layers can be noted at scattering angles near 120°. The phase function values for the bottom layer are much larger than those for the top and middle layers in the scattering region between 5° and 20°. Evidently, the phase function values computed by assuming that cirrus clouds are a homogeneous mixture of particle shapes and sizes are significantly different from the phase functions of the three layers in some specific scattering angle regions.

At 2.11 μm the forward peaks of the phase functions are smaller than at 0.65 μm because the size parameters are smaller. The magnitude of the phase function for side scattering and backscattering angles is much lower at 2.11 μm than at 0.65 μm. The differences between the phase functions for the different layers are enhanced at 2.11 μm because particle absorption is strongly sensitive to the particle sizes. Although not presented for the November 25 case, the overall features of the corresponding phase function analysis are similar to that for the December 5 case.

## 4. Results

### 4.1. Comparison of Reflectance Feature for Two Cirrus Models

The radiative transfer model described in Appendix A is used to compute the bidirectional reflectances for the three-layer and single-layer cirrus models for the purpose of comparing the radiative features of each model. To understand the physics in the comparison, one needs to interpret the scattering geometry involving the Sun and a satellite. For a given solar geometry specified by $(\theta_s, \varphi_s)$ and a viewing geometry specified by $(\theta_v, \varphi_v)$, the corresponding scattering angle is given by

$$\Theta = \cos^{-1}[-\cos\theta_s\cos\theta_v + \sin\theta_s\ \sin\theta_v\cos\phi], \qquad (9)$$

where $\phi = \varphi_s - \varphi_v$ is the relative azimuth angle between Sun and satellite. Note that $\theta_s$ and $\theta_v$ are the inclination angles measured from zenith. Figure 4 illustrates the contours of scattering angles versus solar and view zenith angles for four cases of azimuth angles. The solar zenith and viewing zenith angles range between 0° and 60°. The scattering angles for the region of view-solar geometry considered in the present study are essentially confined to side scattering and backscattering directions. The variational pattern of the scattering angle versus solar zenith and viewing zenith angles depends on the relative azimuth angle. A similar contour diagram of the scattering angle versus $\cos\theta_s$ and $\cos\theta_v$ has been presented by *Mishchenko et al* [1996].

Plate 2 shows the relative difference between the computed bidirectional reflectances of the three-layer and one-layer cirrus models for optically thin cirrus ($\tau = 1$) at 0.65 μm. The relative difference is defined as

$$e(\theta_s,\theta_v,\phi) = 100[R_3(\theta_s,\theta_v,\phi) - R_1(\theta_s,\theta_v,\phi)]/R_1(\theta_s,\theta_v,\phi), \qquad (10)$$

where $R_3$ and $R_1$ are the bidirectional reflection functions computed using the three-layer and one-layer cirrus models, respectively. The maximum difference in this case is about 5%. When the optical thickness is small, the photons originating from single-scattering events dominate the total radiance. The contribution of single-scattering events to the radiance in the three-layer case is given by

$$r(\theta_s,\theta_v,\phi) = \frac{1}{4\cos\theta_s\cos\theta_v}\sum_{l=1}^{3}\left[\tilde{\omega}_l\Delta\tau_l P_l(\theta_s,\theta_v,\phi)\right], \qquad (11)$$

where the summation is carried for all three layers of cirrus. Thus for thin cirrus the bidirectional reflectance function is linearly proportional to the phase function. Referring to Figures 3b and 4, the contours shown in Plate 2 can be explained as follows. For azimuth angles of 0° and 60°, the maximum difference is observed near scattering angles of 120°, which corresponds to the phase function difference at these scattering angles. For azimuth angles of 120° and 180°, the maximum differences for the three-layer and one-layer results are mainly noted near scattering angles of 155° and 180°.

Plate 3 is similar to Plate 2, except that the optical thickness of the cloud is 10. The contribution of multiple scattering increases with increasing optical thickness. The differences occur at scattering angles between 90° and 120°, between 150° and 160°, and between 170° and 180°. From Plates 2 and 3 the difference between the three-layer and one-layer models is within a few percent regardless of optical thickness. Based on these results, modeling the cirrus as a single layer would seem to be sufficient at 0.65 μm.

Plates 4 and 5 are similar to Plates 2 and 3, except that the calculations are performed at 2.11 μm. Absorption by ice at 2.11 μm is much higher than at 0.65 μm. The reflectance obtained using the three-layer model is always larger than that for the one-layer model at 2.11 μm. Because of ice absorption at 2.11 μm, the top layer of cirrus dominates the contribution to the cloud reflectance because photons that penetrate into the lower layers are largely absorbed. The mean size of the ice crystals in

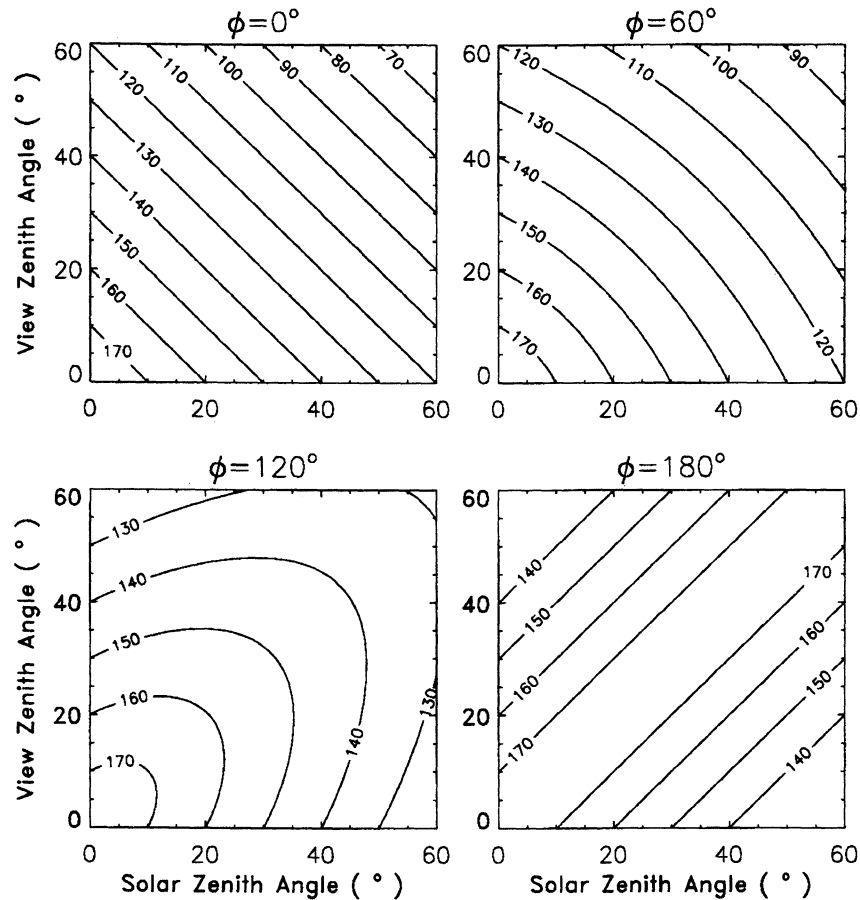## Contours of Scattering Angle



**Figure 4.** The scattering angle versus solar zenith and view zenith angles for four azimuthal angles. Note that the scattering angles are essentially for side scattering and backscattering directions.

the top layer is much smaller than that associated with the general one-layer cirrus model. For a cirrus cloud with a given optical thickness, the cloud reflectance increases with the decrease of mean size of ice crystals. With the increase of optical thickness, the difference between the three-layer and one-layer models increases. For an optical thickness of 10, the differences can reach up to 50%. Because the 2.11 $\mu$m band is used for the retrieval of the mean size and optical depth of cirrus cloud, it is suggested that the vertical inhomogeneity may be important to developing more realistic cirrus retrieval algorithms. In comparing Plates 4 and 5, it may be noted that the difference between the three-layer and one-layer models depends mainly on the scattering angle when the cloud is optically thin. However, for optically thick cirrus, the difference depends not only on scattering angle but also strongly on the viewing zenith and solar zenith angles. This is because the radiance path varies with the solar and view angles. For large solar zenith or viewing zenith angles, the ray path is large and the difference between the three-layer and one-layer cirrus models, and their associated single-scattering properties, becomes more significant.

### 4.2. Sensitivity of Cirrus Reflectance to Shapes of "Quasi-Spherical" Particles

As discussed in section 3.1 regarding the replicator images of ice crystals, the small, so-called "quasi-spherical" ice crystals are

essentially nonspherical. We wish to clarify whether their morphologies can be treated as spheres in light scattering and radiative transfer calculations. It is expected that the answer will depend on the wavelength. At a far infrared wavelength, say, 15 $\mu$m or larger, the nonsphericity of these particles may not be significant because the size parameter becomes small. For a small particle having an effective diameter of 20 $\mu$m, the size parameter is approximately 4 at a wavelength of 15 $\mu$m. In this case, spherical and spheroidal geometries have been used in light scattering computations [e.g., *Sun and Shine*, 1994; *Takano et al.*, 1992]. However, for the 0.65 and 2.11 $\mu$m bands, the size parameter for a small particle having an effective diameter of 20 $\mu$m is approximately 100 and 30 at the band centers, respectively. For a size parameter of this magnitude, the nonsphericity effect of a particle on its scattering properties can be significant.

To investigate the sensitivity of cirrus optical properties to the shapes assumed for the small "quasi-spherical" ice crystals, in this study we compare the results associated with spherical and hexagonal (with an aspect ratio of unity) assumptions for the morphologies of these particles. The "quasi-spherical" particles primarily affect the top and middle layers and are largely absent in the bottom layer. The effective sizes for the top and middle layers are 47 $\mu$m and 92 $\mu$m if hexagonal shapes are used for the "quasi-spherical" particles, whereas the sizes are 52 $\mu$m and

**Table 1.** Single-Scattering Properties of the Top and Middle Layers, Which are Computed in Conjunction With Two Assumptions for the Shapes of the "Quasi-Spherical" Small Ice Crystals (Ice Spheres and Hexagons With Aspect Ratio of 1) [a]

| | λ=0.65 μm | | λ=2.11 μm | |
| --- | --- | --- | --- | --- |
| | Spheres for "Quasi-Spherical" Particles | Hexagons for "Quasi-Spherical" Particles | Spheres for "Quasi-Spherical" Particles | Hexagons for "Quasi-Spherical" Particles |
| | Top Layer | | | |
| $\beta_e$(1/km) | 0 32207 | 0 36926 | 0 33092 | 0 36005 |
| $\tilde{\omega}$ | 0 99999 | 0 99999 | 0 91208 | 0 91335 |
| $g$ | 0 83271 | 0 77965 | 0 86188 | 0 80258 |
| $f_\delta$ | 0 070293 | 0 11689 | 0 038339 | 0 035189 |
| | Middle Layer | | | |
| $\beta_e$(1/km) | 0 41679 | 0.42553 | 0 41837 | 0 42446 |
| $\tilde{\omega}$ | 0 99998 | 0 99998 | 0 85099 | 0 85187 |
| $g$ | 0 81627 | 0 80842 | 0 87949 | 0 86934 |
| $f_\delta$ | 0 12765 | 0 13488 | 0 087641 | 0 086295 |

[a]Note that the shapes of ice crystals with size larger than 50 μm are assumed to be unchanged

95 μm if perfect spherical geometry is assumed for these particles. Evidently, the assumption of shape for the "quasi-spherical" ice crystals in cirrus clouds can lead to a change of effective size by as much as 5 μm.

Table 1 lists the single-scattering properties of the top and middle layers. Substantial differences are noted for delta transmissions at 0.65 μm because of the absence of parallel faces in spheres. The asymmetry factor of the phase function is substantially different at 2.11 μm, showing clearly the dependence of the scattering properties on the assumption of habits. The differences of the results for the two shapes are larger for the top layer than for the middle layer because the former has a larger population of "quasi-spherical" ice crystals.

Figure 5 shows the phase functions associated with the single-scattering properties listed in Table 1. Substantial differences of the phase functions can be seen for the top layer at both the 0.65 and 2.11 μm bands. The overall feature is that the spherical assumption leads to larger phase function values for scattering angles between $10^0$ and 45° and lower values at side scattering angles. However, the spherical assumption leads to a pronounced scattering maximum between 130° and 140°, which corresponds to the rainbow feature of ice spheres. Additionally, the spherical assumption leads to larger phase function values near 180° (backscattering) at 2.11 μm. In the middle layer, the differences caused by the assumption of habit for the small particles are reduced due to the small number of the small particles in the size distribution. Evidently, using the most realistic particle shapes for the small particles in the top layer of cirrus will be crucial to obtaining reliable single-scattering properties of the cloud at 2.11 μm.

Shown in Plates 6 and 7 are the differences between bidirectional reflectances computed using nonspherical hexagonal and spherical geometries in the three-layer cirrus model for thin ($\tau = 1$) and thick ($\tau = 10$) cirrus at the 2.11 μm band. The differences shown in Plates 6 and 7 are defined as

$$e(\theta_s,\theta_v,\phi) = 100[R_{\text{sph}}(\theta_s,\theta_v,\phi)$$
$$- R_{\text{hex}}(\theta_s,\theta_v,\phi)]/R_{\text{hex}}(\theta_s,\theta_v,\phi), \qquad (12)$$

where $R_{\text{sph}}$ and $R_{\text{hex}}$ indicate the reflection functions associated with spherical and hexagonal shapes, respectively, which are assumed for the small "quasi-spherical" ice crystals. The maximum differences shown in Plate 6, which correspond to scattering angles between 130° and 140°, are caused by the rainbow feature of ice spheres. It can also be noted that the assumption of ice spheres leads to an overestimation of reflectance near 180° (backscattering). As optical thickness increases, the contrast decreases for the rainbow feature. However, the enhanced backscattering derived using spheres as the "quasi-spherical" crystal shape is still noticeable. For optically thick cirrus, Plate 7 shows that the assumption of ice spheres for the "quasi-spherical" particles leads to an underestimation of cloud reflection at 2.11 μm except for scattering angles near 180°.

Plates 8 and 9 are similar to Plates 6 and 7, except that the computations have been performed at 0.65 μm. Again, we see pronounced differences between the results associated with the hexagonal and spherical assumptions for the small ice crystals in the uppermost layer. The positive maximum near the backscattering peak noted in Plate 6, however, is not observed in the results shown in Plate 8, because the phase function value for the spheres is less than that of hexagons at 0.65 μm. Additionally, at 0.65 μm a distinct rainbow feature can be noted in the case of thin cirrus. For the optically thick cirrus, the rainbow is blurred due to multiple scattering events occurring within the clouds. Plates 6–9 illustrate that the influence of small-particle shape in the uppermost layer of cirrus is significant at both visible and near-infrared wavelengths.

## 5. Conclusions

In this study we have defined a three-layer cirrus model in terms of ice crystal habit and size distribution based on in situ replicator data acquired during the NASA-sponsored FIRE-II field observation program. We have described a fundamental scattering model and a numerically stable radiative transfer model for the computation of the single-scattering properties of various ice crystals and the bidirectional reflection of cirrus clouds.

We have found that the effect of vertical inhomogeneity within cirrus is not significant at 0.65 μm, a wavelength for which the absorption of ice is negligible. However, in comparison with the one-layer cirrus model, a vertically inhomogeneous cirrus cloud produces substantially larger reflectance at 2.11 μm, a wavelength for which absorption by ice is important. The increase in reflectance occurs because the mean size of ice crystals in the top layer in the three-layer model is smaller than in the case of the one-layer model and the total reflected radiance is dominated by the contribution from the top layer. For a given optical thickness, the reflectance increases with decreasing particle size.

We also investigated the sensitivity of reflection of cirrus clouds to the particle shapes of the "quasi-spherical" ice crystals that have been often assumed to be spheres. For the two cirrus cloud cases presented in this study, the uppermost portion of the cloud tends to be predominantly composed of very small ice crystals. Numerical results have demonstrated that 16e bidirectional reflection function of cirrus is very sensitive to the shape of these particles at both visible and near-infrared wavelengths.
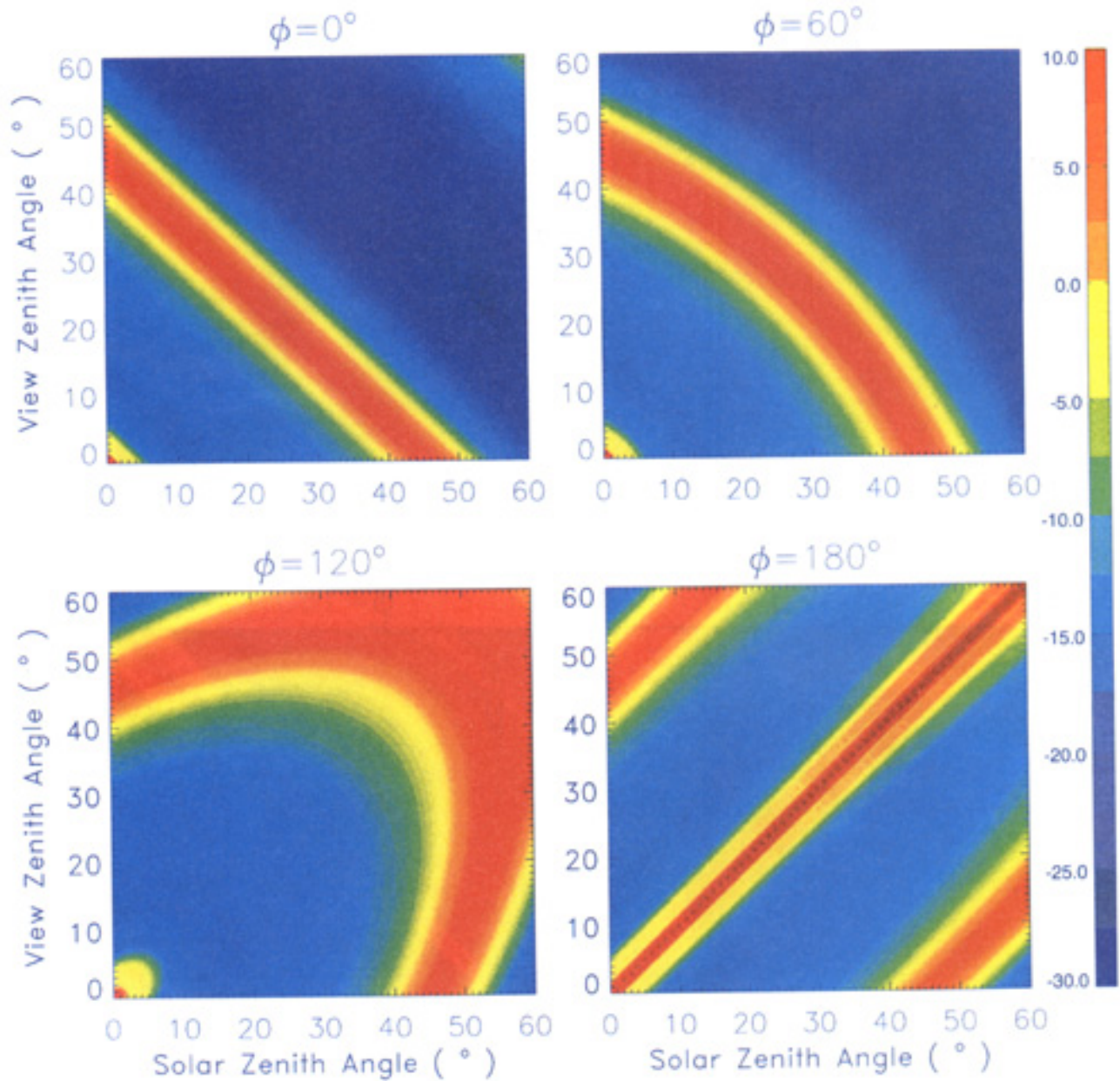
**Plate 6.** The percent relative difference of the bidirectional reflectances computed assuming spherical and hexagonal shapes for the small "quasi-spherical" ice crystals. The difference contours shown are for thin cirrus ($\tau$=1) at MODIS 2.11 μm band. Note the large differences at the ice rainbow and backscattering angles.
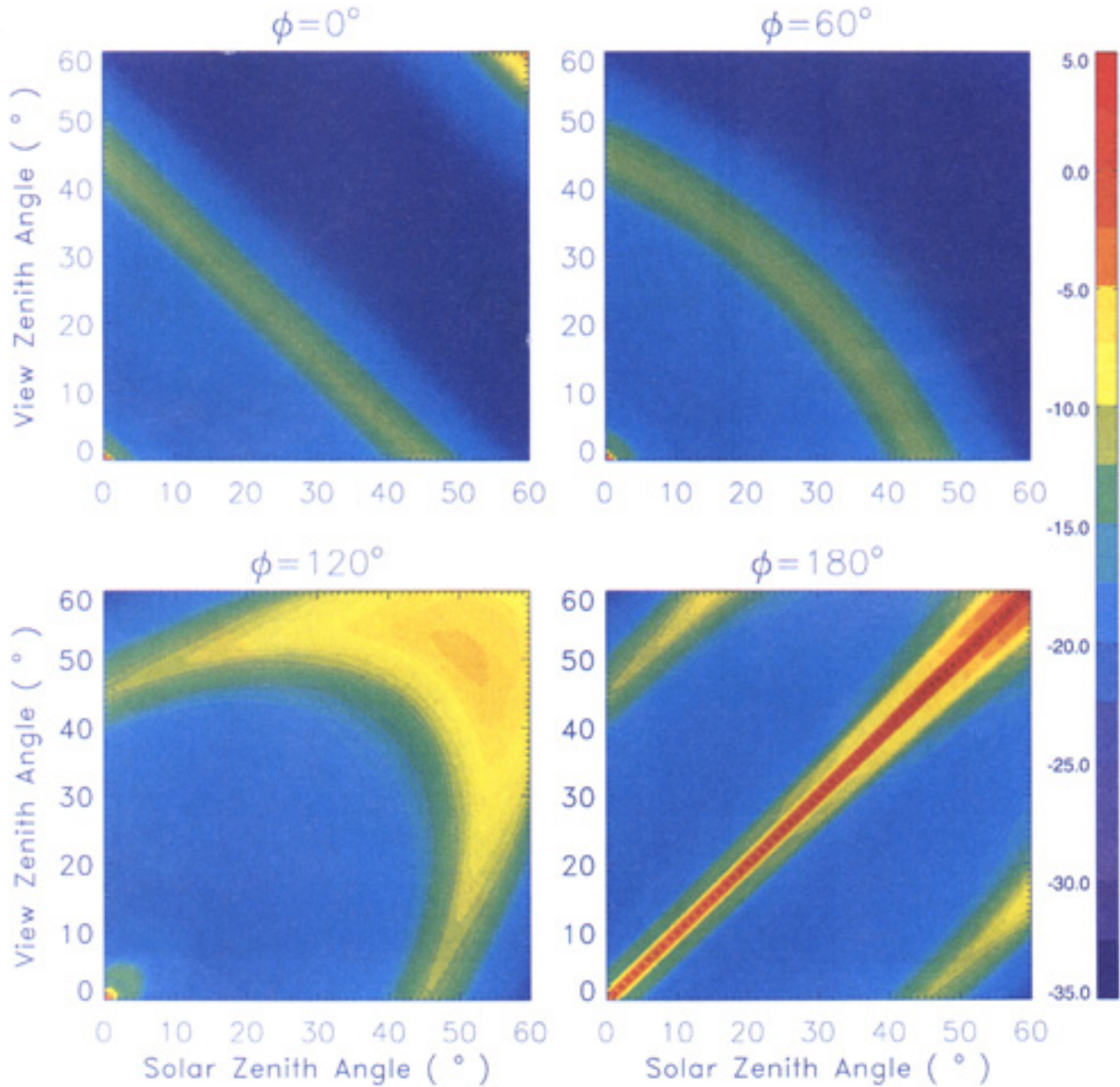
**Plate 7.** Same as Plate 6, except for thick cirrus ($\tau$=10). Note the smoothing of the rainbow maximum.

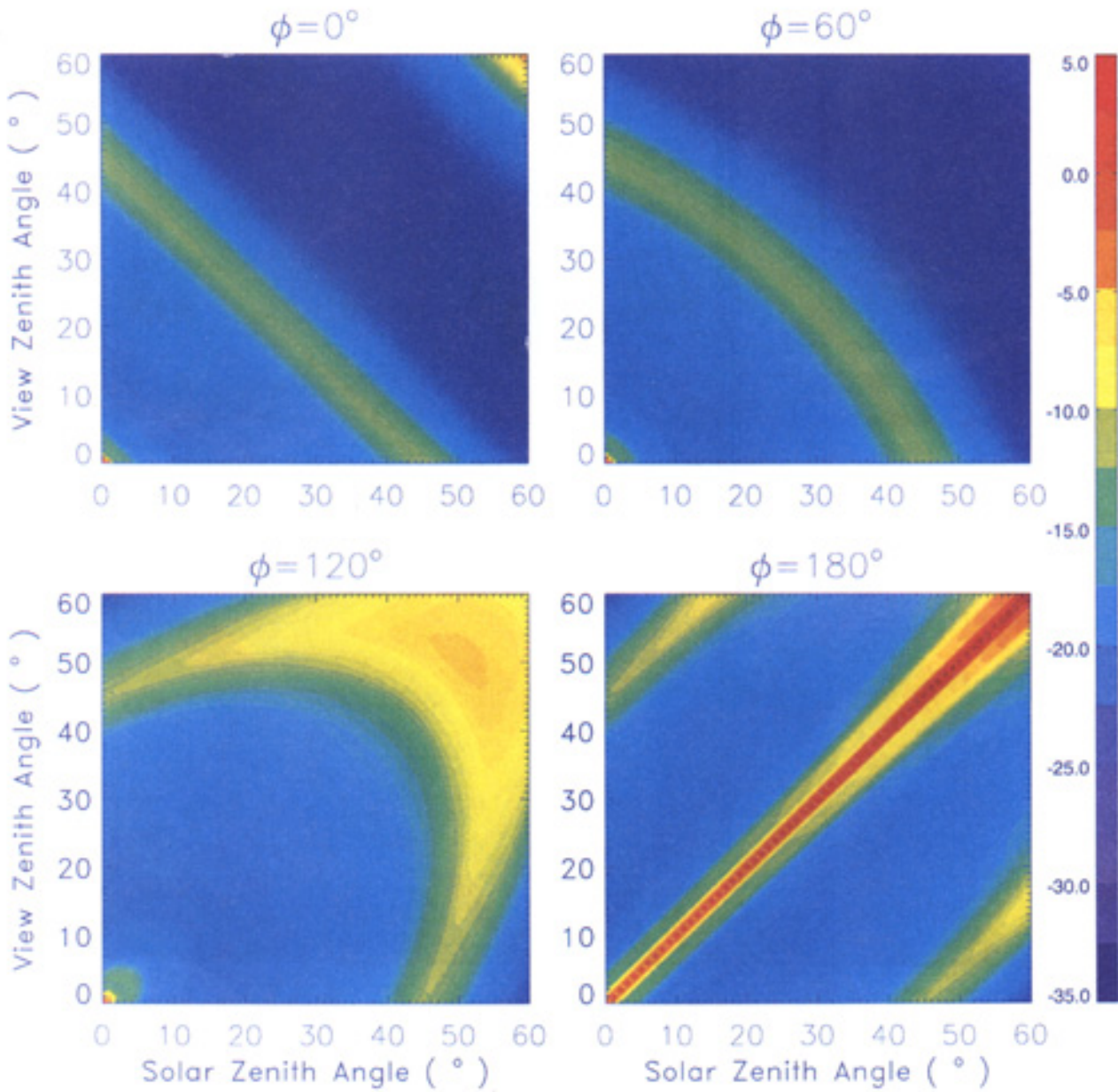**Plate 8.** Same as Plate 6, except for MODIS 0.65 μm band. Note the absence of the positive backscattering angle maximum.
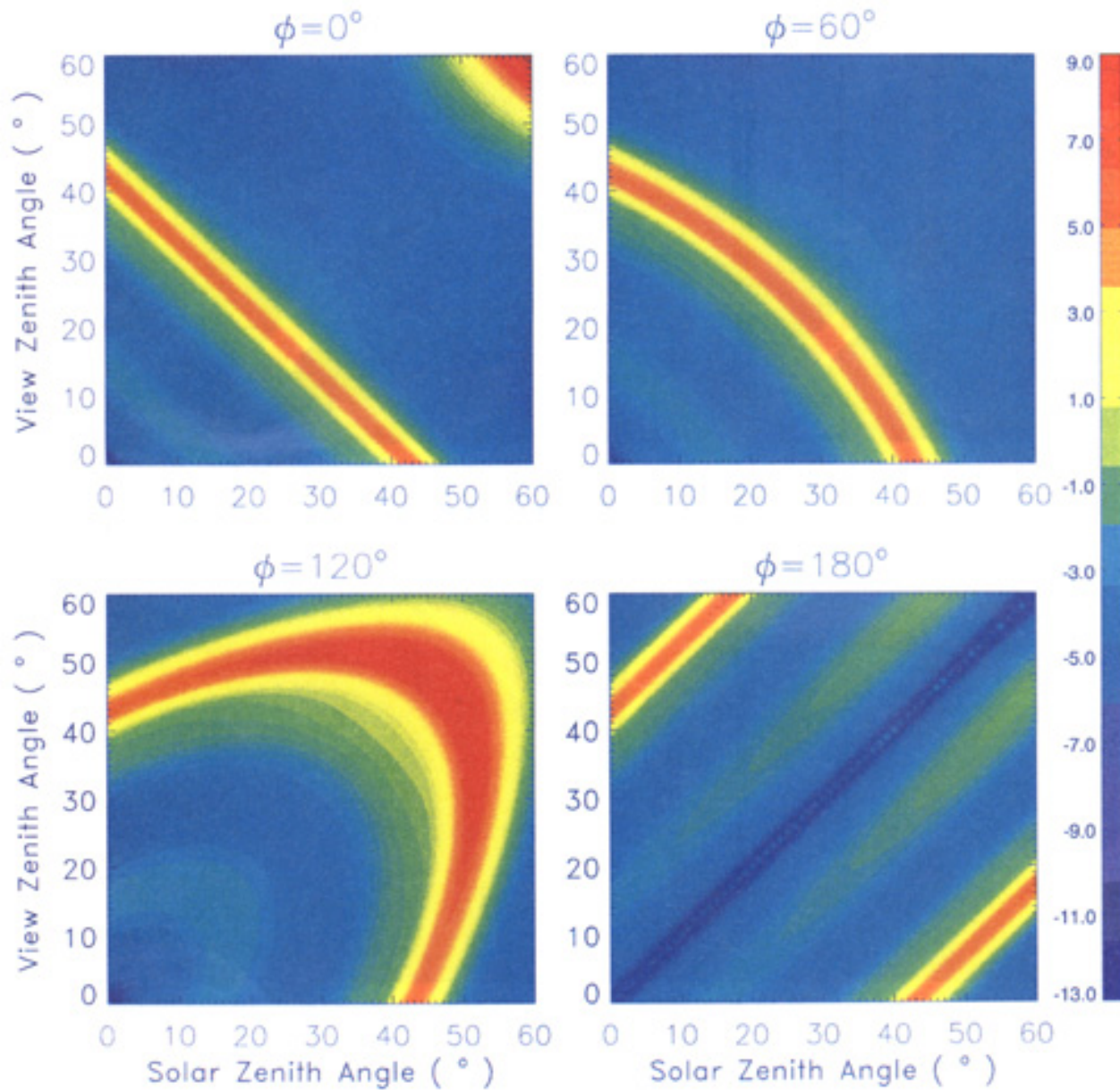
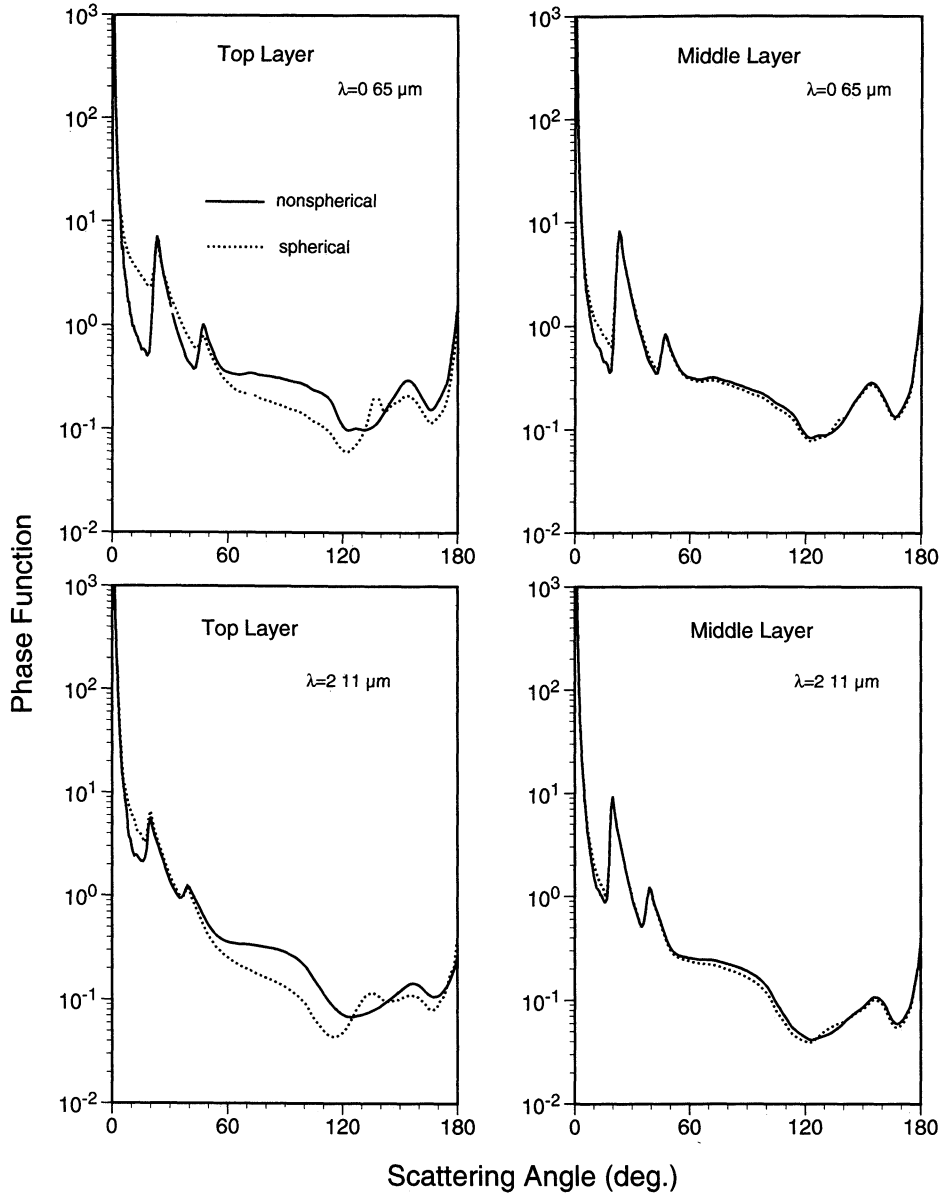**Plate 9.** Same as Plate 8, except for thick cirrus ($\tau$=10).

**Figure 5.** Comparison of the top and middle layer phase functions computed by assuming that the small "quasi-spherical" ice crystals are either spheres or nonspherical hexagons with an aspect ratio of unity. Note the presence of the ice sphere rainbow feature between 130° and 140°.

## Appendix A: Discrete Expression of Adding/Doubling Principle

The adding/doubling method is one of the most robust approaches to solve the radiative transfer equation for multiple-scattering events. The standard mathematical expression of this method involves various tedious angular integrals, although it can be written symbolically in a very simple form. In this section we present a discrete form of the method by introducing a direct transmitting function. As a practical mathematical expression from a computational viewpoint, the discrete adding/doubling equations are straightforward and more efficient in numerical implementation. In addition, the discrete form of the adding/doubling method is more suitable for addressing some numerical concerns, such as the numerical singularity of adding/doubling calculation and the performances of various quadrature schemes.

To economize computational cost and memory requirements, we apply a Fourier expansion over the azimuth angle for radiance and bidirectional reflection and transmission functions:

$$I^{i,r,t}(\mp\mu,\varphi) = \sum_{m=0}^{M} I^{i,r,t(m)}(\mp\mu)\cos m\varphi, \qquad \text{(A1a)}$$

$$I^{i,r,t}(\mu,\varphi,\mu',\varphi') = \sum_{m=0}^{M} r^{(m)}(\mu,\mu')\cos m(\varphi-\varphi'), \qquad \text{(A1b)}$$

$$t(\mu,\varphi,\mu',\varphi') = \sum_{m=0}^{M} t^{(m)}(\mu,\mu')\cos m(\varphi-\varphi'), \qquad \text{(A1c)}$$

where superscripts $i$, $r$, and $t$ indicate incident, reflected, and transmitted intensities, respectively, and $\mu$ and $\mu'$ are positive with allowable values in [0,1]. The maximum number of Fourier terms ($M$) required for the convergent solutions of equations (A1a)–(A1c) depends on the incoming and outgoing radiation

beams as well as the magnitude of the asymmetry of the phase function. For example, only the first term is necessary for a solar zenith angle of 0° (overhead Sun), whereas more than 100 terms may be required for a low solar elevation angle (Sun near the horizon). For solar zenith and viewing zenith angles smaller than 60°, 30 to 40 terms are normally required in the case of cirrus clouds if the strong forward peak of the phase function is truncated. A comprehensive study regarding the number of the terms required in the Fourier series has been carried out by *King* [1983] using the Henyey-Greenstein function and the phase function for a fair weather cumulus.

According to the definitions of reflection and transmission functions [*Hansen and Travis*, 1974], it can be proven that the Fourier components of reflected and transmitted intensities are given by

$$I^{r(m)}(\mu) = (1 + \delta_{m0}) \int_0^1 r^{(m)}(\mu, \mu') I^{i(m)}(-\mu') \mu' \ d\mu', \quad (A2a)$$

$$I^{t(m)}(\mu) = (1 + \delta_{m0}) \int_0^1 t^{(m)}(\mu, \mu') I^{i(m)}(-\mu') \mu' \ d\mu', \quad (A2b)$$

where $\delta_{m0}$ is the Kronecker delta function. It should be pointed out that the radiances defined in equations (A2a) and (A2b) are diffusive intensities, that is, they originate from the scattering of incident radiation by the particles in the scattering layer. If the total (direct + diffuse) transmitted intensity, indicated as $I^t(-\mu, \varphi)$, is defined in the same manner as in the diffusive case, it follows that

$$\tilde{I}^{t(m)}(\mu) = (1 + \delta_{m0}) \int_0^1 \tilde{t}^{(m)}(\mu, \mu') I^{i(m)}(-\mu') \mu' \ d\mu'$$

$$= (1 + \delta_{m0}) \int_0^1 [t^{(m)}(\mu, \mu') + \Delta^{(m)}(\mu, \mu')] I^{i(m)}(-\mu') \mu' \ d\mu', \quad (A3a)$$

where $\tilde{t}(\mu, \mu')$ is the $m$th Fourier component of the total transmission function. $\Delta^{(m)}(\mu, \mu')$ is associated with the transmission of incident radiation and is given by

$$\Delta^{(m)}(\mu, \mu') = \frac{1}{(1 + \delta_{m0}) \mu'} \exp(-\tau / \mu') \delta(\mu - \mu'), \quad (A3b)$$

in which $\delta(\mu - \mu')$ is the Dirac delta function. Evidently, the quantities defined in equations (A2) and (A3) are continuous functions of the arguments $\mu$ and $\mu'$ that range continuously in the interval [0,1]. We select a set of discrete points in the region [0,1] for $\mu$ and $\mu'$; that is, the two variables can only have the values of $\lfloor \mu_1, \mu_2, \cdots \mu_n \rfloor$. With respect to the discrete set, we define the following discrete quantities with single subscript and double subscripts:

$$I_j^{i,t(m)} = I^{i,t(m)}(-\mu_j), \ I_j^{r(m)} = I^{r(m)}(\mu_j), \quad (A4a)$$

$$r_{kj}^{(m)} = r^{(m)}(\mu_j, \mu_k), \ t_{kj}^{(m)} = t^{(m)}(\mu_j, \mu_k), \quad (A4b)$$

$$\tilde{t}_{kj}^{(m)} = \tilde{t}^{(m)}(\mu_j, \mu_k), \ \Delta_{kj}^{(m)} = \Delta^{(m)}(\mu_j, \mu_k). \quad (A4c)$$

Since the continuous region [0,1] is discretized by using a set of points, it is required that an integration of a function $f(\mu)$ with respect to its argument defined in [0,1] be replaced by a discrete summation in the form of

$$\int_0^1 f(\mu) d\mu \rightarrow \sum_{i=1}^n f(\mu_i) W_i, \quad (A5)$$

where $W_i$ are the weights in the summation. For an integral involving the Dirac delta function, the definition of the delta function and equation (A5) lead to the following relationship:

$$f(\mu_i) = \int_0^1 f(\mu) \delta(\mu - \mu_i) d\mu \rightarrow \sum_{j=1}^n f(\mu_j) W_j \delta(\mu_j - \mu_i). \quad (6)$$

Evidently, to guarantee the equality in equation (A6) in the discrete procedure, the Dirac delta function should be replaced by Kronecker symbol in the form of

$$\delta(\mu_j - \mu_i) \rightarrow \delta_{ji} / W_j = 1 / W_j \ j = 1, \quad (A7a)$$

$$\delta(\mu_j - \mu_i) \rightarrow \delta_{ji} / W_j = 0 \quad j \neq 1. \quad (A7b)$$

Thus the direct transmission function in discrete form is given by

$$\Delta_{ij}^{(m)}(\tau) = \frac{1}{(1 + \delta_{m0}) W_j \mu_j} \exp(-\tau / \mu_j) \delta_{ij}. \quad (A8)$$

For the discrete quantities defined with respect to the set of discrete points $\lfloor \mu_1, \mu_2, \cdots \mu_n \rfloor$, we introduce a mathematical operator $\otimes$ defined by

$$A_{ij}^{(m)} \otimes B_{jk}^{(m)} = (1 + \delta_{m0}) \sum_{j=1}^n A_{ij}^{(m)} B_{jk}^{(m)} \mu_j W_j, \quad (A9a)$$

$$C_j^{(m)} \otimes B_{jk}^{(m)} = (1 + \delta_{m0}) \sum_{j=1}^n C_j^{(m)} B_{jk}^{(m)} \mu_j W_j. \quad (A9b)$$

The operator $\otimes$ is similar to an ordinary matrix multiplication except that a weight is included in the former. Thus for one homogeneous layer, the reflected, diffusely transmitted, and total transmitted radiances are related to the incident radiation via the following relationships:

$$I_k^{r(m)} = I_j^{i(m)} \otimes r_{jk}^{(m)},$$

$$I_k^{t(m)} = I_j^{i(m)} \otimes t_{jk}^{(m)}, \ \tilde{I}_k^{t(m)} = I_j^{i(m)} \otimes \tilde{t}_{jk}^{(m)}. \quad (A10)$$

One of the interesting features of using the operator $\otimes$ is the variation of subscripts in the expressions in equation (A10): The incident beam denoted by subscript $j$ is redirected to the direction denoted by subscript $k$ after interacting with the scattering layer. Similarly, for two layers indicated by superscripts $a$ and $b$, we have the following relationships:

$$I_k^{r(m)} = I_j^{i(m)} \otimes [r_{jk}^{a(m)} + \tilde{t}_{jk}^{a(m)} \otimes U_{ln}^{(m)} \otimes \tilde{t}_{nk}^{a*(m)}], \quad (A11a)$$

and

$$\tilde{I}_k^{t(m)}$$

$$= I_j^{i(m)} \otimes [\tilde{t}_{jl}^{a(m)} \otimes \tilde{t}_{lk}^{b(m)} + \tilde{t}_{jl}^{a(m)} \otimes D_{ln}^{(m)} \otimes \tilde{t}_{nk}^{b(m)}], \quad (A11b)$$

where the asterisk indicates that the transmission function corresponds to the case of illumination coming from below. The quantities $D$ and $U$ in equations (A11a) and (A11b) are given by

$$D_{ij}^{(m)} = \sum_{n=1}^n D_{ij}^{(m),(n)}, \ U_{ij}^{(m)} = r_{ij}^{b(m)} + D_{il}^{(m)} \otimes r_{lj}^{b(m)}, \quad (A12a)$$

$$D_{ij}^{(m),(n+1)} = D_{il}^{(m),(n)} \otimes D_{lj}^{(m),(1)},$$

$$D_{ij}^{(m),(1)} = r_{il}^{b(m)} \otimes r_{lj}^{a*(m)}. \quad (A12b)$$

According to the sensitivity study by *Hansen and Travis* [1974], we use $N = 12$, 5, and 3 in the summation involved in the first expression in equation (A12a) for $m < 10$, $10 < m < 100$, and $m > 100$, respectively. The remaining terms are approximated by a geometric series. The physics of the adding/doubling principle can be viewed clearly in terms of the variations of the subscripts from left to right in the right-hand sides of equations (A11a) and (A11b). The reflection and transmission functions for the combined layer are given by

$$R_{jk}^{(m)} = r_{jk}^{a(m)} + \tilde{t}_{jl}^{a(m)} \otimes U_{ln}^{(m)} \otimes \tilde{t}_{nk}^{a*(m)}, \quad (A13a)$$

and

$$\tilde{T}_{jk}^{(m)} = \tilde{t}_{jl}^{a(m)} \otimes \tilde{t}_{lk}^{b(m)} + \tilde{t}_{jl}^{a(m)} \otimes D_{ln}^{(m)} \otimes \tilde{t}_{nk}^{b(m)}. \quad \text{(A13b)}$$

The transmission function given in equation (A13b) contains the contribution due to direct transmission, which is implicitly in the form of a delta function, and it may potentially cause inaccuracy in numerical computation. Thus it is necessary to separate the diffusive and direct components in equation (A13b). It is noted that

$$\tilde{t}_{jl}^{a(m)} \otimes \tilde{t}_{lk}^{b(m)} = [t_{jl}^{a(m)} + \Delta_{jl}^{(m)}(\tau_a)] \otimes [t_{lk}^{b(m)} \\ + \Delta_{lk}^{(m)}(\tau_b)] = t_{jl}^{a(m)} \otimes t_{lk}^{b(m)} + \exp(-\tau_a / \mu_j) t_{jk}^{b(m)} \\ + t_{jk}^{a(m)} \exp(-\tau_b / \mu_k) + \Delta_{jk}^{(m)}(\tau_a + \tau_b). \quad \text{(A14)}$$

Thus the diffusive transmission function for the combined layer is given by

$$T_{jk}^{(m)} = t_{jl}^{a(m)} \otimes t_{lk}^{b(m)} + t_{jk}^{a(m)} \exp(-\tau_b / \mu_k) \\ + \exp(-\tau_a / \mu_j) t_{jk}^{b(m)} + \tilde{t}_{jl}^{a(m)} \otimes D_{ln}^{(m)} \otimes \tilde{t}_{nk}^{b(m)}. \quad \text{(A15)}$$

Equations (A12a), (A12b), (A13a), and (A15) constitute the adding/doubling equations. It should be pointed that the matrix associated with direct transmission is diagonal. In numerical computation the numerical efficiency and accuracy can be improved substantially if the multiplication of the direct transmission function with another quantity is evaluated analytically, such as

$$\Delta_{ij}^{(m)}(\tau) \otimes A_{jk}^{(m)} = \exp(-\tau / \mu) A_{jk}^{(m)}, \quad A_{jk}^{(m)} \otimes \Delta_{ki}^{(m)}(\tau) \\ = A_{jk}^{(m)} \exp(-\tau / \mu_k). \quad \text{(A16)}$$

As mentioned in preceding discussions, the continuous integration involved in the adding/doubling calculation must be replaced by a proper quadrature scheme. Mathematically, we need to select proper pairs of $(\mu_i, W_i)$ for the definition of the mathematical operator $\otimes$ in equations (A9a) and (A9b). The most popular quadrature schemes are Gauss, Lobatto, and Radau quadrature schemes [*Press et al.*, 1986; *Hildebrand*, 1974]. For the angular region involved, these three schemes cover $\mu$ (or $\mu'$) $\in$ (0,1), [0,1], and (0,1), respectively. That is, Gaussian quadrature is open at both ends, Labotto quadrature is closed at both 0 and 1, and the Radau scheme is open at 0 but closed at 1. The radiance data at nadir view are usually required in retrieval applications. Thus an extrapolation must be used to obtain the nadir view radiance if Gaussian quadrature is used. The disadvantage of using Gaussian quadrature in radiative transfer calculation has also been noted by *Mishchenko* et al. [1999]. Although the Labotto scheme is closed at both ends of the integral region, the information at $\mu = 0$ actually does not make any contribution to the angular integration, as is evident from equations (A9a) and (A9b). In addition, including $\mu = 0$ will cause a singularity in the initialization of the adding/doubling calculation. Therefore we use the Radau scheme in the present study.

To initialize the adding/doubling process, we start with a very thin homogeneous layer with optical depth $\Delta\tau$ ($\sim 10^{-8}$). The reflection and transmission truncation for this layer can be obtained on the basis of the invariance principle [*Hansen and Travis*, 1974] as follows:

$$r_{i,j}^{(m)} = \frac{\tilde{\omega}\Delta\tau}{4\mu_i\mu_j}\left[1 - \frac{\Delta\tau}{2}\frac{\mu_i + \mu_j}{\mu_i\mu_j}\right]P_{i,j}^{r(m)} \\ + \frac{\tilde{\omega}^2\Delta\tau^2}{32\mu_i\mu_j}\Big[(P_{ik}^{r(m)} / \mu_k) \otimes (P_{kj}^{t(m)} / \mu_k) \\ + (P_{ik}^{t(m)} / \mu_k) \otimes (P_{kj}^{r(m)} / \mu_k)\Big], \quad \text{(A17a)}$$

$$t_{i,j}^{(m)} = \frac{\tilde{\omega}\Delta\tau}{4\mu_i\mu_j}\left[1 - \frac{\Delta\tau}{2}\frac{\mu_i + \mu_j}{\mu_i\mu_j}\right]P_{i,j}^{t(m)} \\ + \frac{\tilde{\omega}^2\Delta\tau^2}{32\mu_i\mu_j}\Big[(P_{ik}^{t(m)} / \mu_k) \otimes (P_{kj}^{t(m)} / \mu_k) \\ + (P_{ik}^{r(m)} / \mu_k) \otimes (P_{kj}^{r(m)} / \mu_k)\Big]. \quad \text{(A17b)}$$

In equations (A17a) and (A17b), $P_{ij}^{r(m)}$ and $P_{ij}^{t(m)}$ are defined as follows:

$$P_{ij}^{r(m)} = \sum_{l=m}^{M}(2 - \delta_{m0})\tilde{\omega}_l\tilde{P}_l^m(-\mu_i)\tilde{P}_l^m(\mu_j) \\ = \sum_{l=m}^{M}(2 - \delta_{m0})\tilde{\omega}_l\tilde{P}_l^m(\mu_i)\tilde{P}_l^m(-\mu_j), \quad \text{(A18a)}$$

$$P_{ij}^{t(m)} = \sum_{l=m}^{M}(2 - \delta_{m0})\tilde{\omega}_l\tilde{P}_l^m(\mu_i)\tilde{P}_l^m(\mu_j), \quad \text{(A18b)}$$

in which $\tilde{\omega}_l$ is given by

$$\tilde{\omega}_l = \frac{2l+1}{2}\int_{-1}^{1}P(\mu)P_l(\mu)d\mu \\ = \frac{2l+1}{2}\int_{0}^{1}[P(\mu) + (-1)^l P(-\mu)]P_l(\mu)d\mu, \quad \text{(A19)}$$

where $P(\mu)$ is the phase function and $P_l(\mu)$ is the Legendre polynomial of $l$th order. In numerical computation we use the Radau quadrature scheme for the integration in equation (A19). Thus phase function information at the exact forward and backward directions is accounted for. The function $P_l^m$ in equations (A18a) and (A18b) are the "renormalized" (or referred to as the "normalized" in DISORT (ftp://climate.gsfc.nasa.gov/pub/wiscombe/Multiple_Scatt/DISO RT_1.21DISORTReport.pdf)) associated Legendre polynomials first introduced by *Dave and Armstrong* [1970], defined as

$$\tilde{P}_l^m(\mu) = \sqrt{\frac{(l-m)!}{(l+m)!}}P_l^m(\mu), \quad \text{(A20)}$$

where $P_l^m$ is the ordinary Legendre function. The normalized associated Legendre functions can be calculated on the basis of the following recurrence relationship:

$$\tilde{P}_{l+1}^m(\mu) = \frac{2l+1}{\sqrt{(l+m+1)(l-m+1)}}\mu\tilde{P}_l^m(\mu) \\ - \sqrt{\frac{(l+m)(l-m)}{(l+m+1)(l-m+1)}}\tilde{P}_{l-1}^m(\mu), \quad \text{(A21a)}$$

with the two initial values for the preceding recurrence given by

$$\tilde{P}_m^m(\mu) = (-1)^m\sqrt{\frac{(2m-1)!!}{(2m)!!}}(1 - \mu^2)^{m/2}, \\ \tilde{P}_{m+1}^m(\mu) = \mu\sqrt{2m+1}\,\tilde{P}_m^m(\mu). \quad \text{(A21b)}$$

23

Note that alternatives for initializing the preceding recurrence can be found in the paper by *Dave and Armstrong* [1970] and a technical report for DISORT (URL is given before equation (A20)). It should be pointed out that in many references the phase function expansion based on Legendre polynomials is given in the form of

$$P^{(m)}(\mu_i, \mu_j)$$

$$= \sum_{l=m}^{M} (2 - \delta_{m0}) \, \tilde{\omega}_l \frac{(l-m)!}{(l+m)!} P_l^m(\mu_i) P_l^m(\mu_j), \qquad \text{(A22a)}$$

where the associated Legendre polynomial or Legendre functions can be calculated on the basis of the following recursive relationship:

$$P_{l+1}^m(\mu) = \frac{(2l+1)\mu P_l^m(\mu) - (l+m)P_{l-1}^m(\mu)}{l-m+1}. \qquad \text{(A22b)}$$

The factor $(l-m)!/(l+m)!$ in equation (A22a) rapidly reduces to zero, while the values of Legendre functions are very large for a large m with $l \geq m$, as noted by *Dave and Armstrong* [1970]. For this reason the preceding approach given by equations (A22a) and (A22b) for the expansion of the phase function in radiative transfer simulations is not numerically stable, in particular, when the asymmetry of phase function is substantial and higher-order Legendre functions are required in the phase function expansion.

Since the predominant sizes of ice crystals in cirrus clouds are much larger than visible and near-infrared wavelengths, there is a strong forward peak in the corresponding phase function. To include this forward peak in numerical computations, thousands of terms may be required in the Fourier expansions involved in equations (A1a)-(A1c) for a general solar view geometry, and also in the phase function expansion given by equations (A18a) and (A18b). It should be pointed that the number of radiance streams used in the adding/doubling calculation needs to increase with the increase of the terms used in the phase function expansion so that the orthogonality of the selected finite set of Legendre functions in a discrete form can be guaranteed. Thus the strong forward peak makes the numerical computation impractical. For this reason the strong forward peaks of phase functions are truncated in practice. The schemes used for the truncation are diverse, and have been evaluated in an extensive discussion by *Wiscombe* [1977], who has further developed the $\delta - M$ method in order to avoid the shortcomings pertaining to various ad hoc empirical approaches. For truncating the forward peak of the phase function involved in this study, we employ the method developed by *Hu et al.* [2000], which is an extension of the $\delta - M$ method. After the phase function is truncated, the single-scattering properties need to be adjusted on the basis of the similarity principle [*Wiscombe*, 1977; *van de Hulst*, 1980; *Takano and Liou*, 1989b]. For example, optical depth and single-scattering albedo are adjusted as follows:

$$\tau' = (1 - f\tilde{\omega})\tau, \quad \tilde{\omega}' = (1 - f)\tilde{\omega}/(1 - f\tilde{\omega}), \qquad \text{(A23)}$$

where $f$ is the fraction of energy associated with the truncated forward peak.

## References

Ackerman, S. A, W L Smith, J. D Spinhirne, and H E. Revercomb, The 27-28 October 1986 FIRE IFO cirrus case study: Spectral properties of cirrus clouds in the 8-12 μm window, *Mon Weather Rev.*, 118, 2377-2388, 1990.

Ackerman, S. A., K I. Strabala, W. P Menzel, R A Frey, C C Moeller, and L. E. Gumley, Discriminating clear sky from clouds with MODIS, *J Geophys Res.*, 103, 32,141-32,157, 1998

Arnott, W P., Y Y Dong, J Hallett, and M R Poellot, Role of small ice crystals in radiative properties of cirrus: A case study, FIRE II, November 22, 1991, *J Geophys Res*, 99, 1371-1381, 1994.

Baum, B A., D Kratz, P Yang, S C Ou, Y X Hu, P F Soulen, and S C. Tsay, Remote sensing of cloud properties using MODIS airborne simulator imagery during SUCCESS, 1, Data and models, *J Geophys Res*, 105, 11,767-11,780, 2000a

Baum, B A., P. F Soulen, K. I Strabala, M D King, S A Ackerman, W P. Menzel, and P Yang, Remote sensing of cloud properties using MODIS airborne simulator imagery during SUCCESS, 2, Cloud thermodynamic phase, *J Geophys Res*, 105, 11,781-11,792, 2000b

Cox, C, and W Munk, Measurement of the roughness of the sea surface from photographs of the Sun's glitter, *J Opt Soc Am*, 44, 838-850, 1954

Cross, J D, Study of the surface of ice with a scanning electron microscope, in *Physics of Ice, Proceedings of the International Symposium on the Physics of Ice*, pp 81-94, Plenum, New York, 1968

Dave, J.V, and B Armstrong, Computations of high-order associated Legendre polynomials, *J Quant Spectrosc Radiat Transfer*, 10, 557-562, 1970

Foot, J. S., Some observations of the optical properties of clouds, II, Cirrus, *Q. J. R. Meteorol Soc.*, 114, 145-164, 1988.

Francis, P N., Some aircraft observations of the scattering properties of ice crystals, *J Atmos. Sci.*, 52, 1142-1154, 1995

Francis, P. N., A. Jones, R. W Saunders, K. P Shine, A Slingo, and Z Sun, An observational and theoretical study of the radiative properties of cirrus Some results from ICE'89, *Q J R Meteorol Soc.*, 120, 809-848, 1994

Fu, Q., An accurate parameterization of the solar radiative properties of cirrus clouds for climate models, *J Clim*, 9, 2058-2082, 1996

Gao, B. C, and Y J Kaufman, Selection of 1 375 μm MODIS channel for remote sensing of cirrus clouds and stratospheric aerosols from space, *J Atmos. Sci.*, 52, 4231-4237, 1995

Gayet, J F, O Crepel, and J F Fournol, A new polar nephelometer for in situ measurements of microphysical and optical properties of clouds, in *Proceedings of the Conference on Cloud Physics*, pp 26-30, Am Meteorol Soc, Boston, Mass, 1995

Hansen, J E., and J B Travis, Light scattering in planetary atmospheres, *Space Sci Rev*, 16, 527-610, 1974.

Heymsfield, A J, and J Iaquinta, Cirrus crystal terminal velocities, *J. Atmos Sci.*, 57, 916-938, 2000

Heymsfield, A. J., and C. M. R. Platt, A parameterization of the particle size spectrum of ice clouds in terms of the ambient temperature and the ice water content, *J. Atmos. Sci*, 41, 846-855, 1984

Hildebrand, E. B, *Introduction to Numerical Analysis*, Dover, Mineola, N Y., 1974

Hu, Y X, and K. Stamnes, An accurate parameterization of the radiative properties of water clouds suitable for use in climate models, *J Clim*, 6, 728-742, 1993

Hu, Y. X., B Wielicki, B Lin, G Gibson, S C Tsay, K. Stamnes, and T Wong, Delta-fit: A fast and accurate treatment of particle scattering phase functions with weighted singular-value decomposition least-square fitting, *J Quant. Spectrosc Radiat Transfer*, 65, 681-690, 2000

Hunt, G. E, and I. P Grant, Discrete space theory of radiative transfer and its application to problems in planetary atmospheres, *J Atmos Sci.*, 26, 963-972, 1966

Inoue, T, On the temperature and effective emissivity determination of semi-transparent cirrus clouds by bispectral measurements in the 10 μm region, *J Meteorol Soc Jpn.*, 63, 88-99, 1985

King, M D, Number of terms required in the Fourier expansion of the reflection function for optical thick atmospheres, *J Quant Spectrosc Radiat Transfer*, 30, 143-161, 1983

King, M. D., Y J Kaufman, W P Menzel, and D. Tanre, Remote sensing of cloud, aerosol, and water vapor properties from the Moderate Resolution Imaging Spectrometer (MODIS), *IEEE Trans Geosci. Remote Sens.*, 30, 2-27, 1992

24

King, M. D., S -C Tsay, S. E Platnick, M Wang, and K N Liou, Cloud retrieval algorithms for MODIS Optical thickness, effective particle radius, and thermodynamic phase, MODIS Algorithm Theoretical Basis Document, 79 pp, NASA Goddard Space Flight Cent, Greenbelt, Md, 1997

Lenoble, J (Ed), *Radiative Transfer in Scattering and Absorbing Atmospheres: Standard Computational Procedures*, A Deepak, Hampton, Va, 1985.

Liou, K. N., Influence of cirrus clouds on weather and climate processes A global perspective, *Mon Weather Rev*, *114*, 1167-1199, 1986

Liou, K N, S C Ou, Y Takano, F P J Valero, and T. P Ackerman, Remote sounding of the tropical cirrus cloud temperature and optical depth using 6 5 and 10 6 µm radiometers during STEP, *J Appl Meteorol*, *29*, 716-726, 1990

Mace, G. G., T. Ackerman, E. E Clothiaux, and B A Albrecht, A study of composite cirrus morphology using data from a 94-GHz radar and correlations with temperature and large-scale vertical motion, *J Geophys. Res.*, *102*, 13,581-13,593, 1997

Macke, A, J Muller, and E Rascke, Single-scattering properties of atmospheric crystals, *J Atmos. Sci.*, *53*, 2813-2825, 1996

McFarquhar, G M., and A J Heymsfield, Microphysical characteristics of three cirrus anvils sampled during the Central Equatorial Pacific Experiment (CEPEX), *J Atmos Sci*, *52*, 4143-4158, 1996

McFarquhar, G M, and A. J Heymsfield, Parameterization of tropical cirrus ice crystal size distributions and implications for radiative transfer: Results from CEPEX, *J Atmos Sci*, *54*, 2187-2200, 1997

Miloshevich, L. M, and A. J Heymsfield, A balloon-borne continuous cloud particle replicator for measuring vertical profiles of cloud microphysical properties Instrument design, performance, and collection efficiency analysis, *J Atmos Oceanic Technol*, *14*, 753-768, 1997

Minnis, P, K. N Liou, and Y Takano, Inference of cirrus cloud properties using satellite-observed visible and infrared radiances, I, Parameterization of radiance fields, *J Atmos Sci*, *50*, 1279-1304, 1993a

Minnis, P, K N Liou, and Y Takano, Inference of cirrus cloud properties using satellite-observed visible and infrared radiances, II, Verification of theoretical cirrus radiative properties, *J Atmos Sci*, *50*, 1305-1322, 1993b

Mishchenko, M. I., and A Macke, Incorporation of physical optics effects and computation of the Legendre expansion for ray-tracing phase functions involving δ-function transmission, *J Geophys Res*, *103*, 1799-1805, 1998

Mishchenko, M. I, W. B Rossow, A. Macke, and A. A Lacis, Sensitivity of cirrus cloud albedo, *bidirectional* reflectance and optical thickness retrieval accuracy to ice particle shape, *J Geophys Res*, *101*, 16,973-16,985, 1996

Mishchenko, M I, J. M Dlugach, E. G *Yanovitskij*, and N T Zakharova, Bidirectional reflectance of flat, optically thick particulate layers: An efficient radiative transfer solution and applications to snow and soil surfaces, *J Quant. Spectrosc Radiat Transfer*, *63*, 409-432, 1999

Mitchell, D L, S K Chai, Y Liu, A J Heymsfield, and Y Dong, Modeling cirrus clouds, I, Treatment of bimodal size spectra and case study analysis, *J Atmos Sci*, *53*, 2952-2966, 1996a

Mitchell, D L., A Macke, and Y. Liu, Modeling cirrus clouds, II, Treatment of radiative properties of radiative properties, *J Atmos Sci.*, *53*, 2967-2988, 1996b.

Nakajima, T., and M. D. King, Determination of the optical thickness and effective particle radius of clouds from reflected solar radiation measurements, I, Theory, *J Atmos Sci*, *47*, 1878-1893, 1990

Ohtake, T, Unusual crystals in ice fog, *J Atmos Sci*, *27*, 509-511, 1970

Ou, S. C., K. N Liou, W. M Gooch, and Y Takano, Remote sensing of cirrus cloud properties using AVHRR 3 7 and 10 9 µm channels, *Appl Opt.*, *32*, 2171-2180, 1993

Posse, P, and W von Hoyningen-Huene, Information about scattering properties and particle characteristics of a stratiform cloud at Helgoland by remote optical measurements, *Beitr. Phys Atmos*, *68*, 359-366, 1995

Press, W. H, B P Flannery, S A Teukolsky, and W T Vetterling, *Numerical Recipes*, 839 pp, Cambridge Univ. Press, New York, 1986

Rossow, W B, and A. A Lacis, Global seasonal cloud variations from satellite radiance measurements, II, Cloud properties and radiative effects, *J Clim*, *47*, 2488-2503, 1990

Stamnes, K., S -C Tsay, W Wiscombe, and K Jayaweera, Numerically stable algorithm for discrete-ordinate-method radiative transfer in multiple scattering and emitting layered media, *Appl Opt*, *27*, 2502-2509, 1988

Starr, D O, A cirrus cloud experiment Intensive field observations planned for FIRE, *Bull Am Meteorol. Soc*, *68*, 119-124, 1987

Stephens, G L, S C Tsay, P W Stackhouse, and P J Flatau, The relevance of the microphysical and radiative properties of cirrus clouds to climate and climate feedback, *J Atmos Sci*, *47*, 1742-1753, 1990

Strabala, K I, S. A. Ackerman, and W P Menzel, Cloud properties inferred from 8-12 µm data, *J Appl Meteorol*, *2*, 212-229, 1994

Sun, Z, and K P Shine, Studies of the radiative properties of ice and mixed-phase clouds, *Q J R Meteorol Soc*, *120*, 407-426, 1994

Takano, Y, and K N Liou, Radiative transfer in cirrus clouds, I, Single-scattering and optical properties of hexagonal ice crystals, *J Atmos Sci*, *46*, 3-19, 1989a

Takano, Y, and K N Liou, Radiative transfer in cirrus clouds, II, Theory and computation of multiple scattering in an anisotropic medium, *J Atmos Sci*, *46*, 20-36, 1989b

Takano, Y., K N. Liou, and P Minnis, The effects of small ice crystals on cirrus infrared radiative properties, *J Atmos Sci*, *49*, 1487-1493, 1992

Thuman, W C, and E Robinson, Studies of Alaskan ice-fog particles, *J Meteorol*, *11*, 151-156, 1954

Twomey, S, Matrix methods for multiple scattering problems, *J Atmos Sci*, *23*, 289-296, 1966

van de Hulst, H C, *Light Scattering by Small Particles*, 470 pp, John Wiley, New York, 1957

van de Hulst, H C, *Multiple Light Scattering*, 739 pp, Academic, San Diego, Calif, 1980

Wielicki, B A, J T Suttles, A J Heymsfield, R M Welch, J D Spinhire, M L. C Wu, and D O Starr, The 27-28 October 1986 FIRE IFO cirrus case study Comparison of radiative transfer theory with observations by satellite and aircraft, *Mon Weather Rev*, *118*, 2356-2376, 1990.

Wiscombe, W J, The delta-M method: Rapid yet accurate radiative flux calculations for strongly asymmetric phase functions, *J Atmos Sci*, *34*, 1408-1422, 1977

Wyser, K, and P. Yang, Average ice crystal size and bulk short-wave single-scattering properties of cirrus clouds, *Atmos Res*, *49*, 315-335, 1998

Yang, P, and K N Liou, Light scattering by hexagonal ice crystals Comparison of finite-difference time domain and geometric optics model, *J Opt Soc Am A*, *12*, 162-176, 1995

Yang, P, and K N Liou, Geometric-optics-integral-equation method for light scattering by nonspherical ice crystals, *Appl. Opt.*, *35*, 6568-6584, 1996

Yang, P, and K N Liou, Light scattering by hexagonal ice crystals: Solution by ray-by-ray integration algorithm, *J Opt Soc Am A*, *14*, 2278-2289, 1997

Yang, P, and K N Liou, Single-scattering properties of complex ice crystals in terrestrial atmosphere, *Contrib Atmos Phys*, *71*, 223-248, 1998

B A Baum, and Y X Hu, Atmospheric Sciences Division, MS 420, NASA Langley Research Center, Hampton, VA 23681

B -C Gao, Remote Sensing Division, code 7212, U S Naval Research Laboratory, Washington, D C 20375

A J Heymsfield, G M McFarquhar, and L M Miloshevich, National Center for Atmospheric Research, Boulder, CO 80307

S L Nasiri, Cooperative Institute for Meteorological Satellite Studies, University of Wisconsin-Madison, 1225 West Dayton Street, Madison, WI 53706

P F Soulen, W J Wiscombe, and P Yang, Code 913, NASA Goddard Space Fight Center, Greenbelt, MD 20771 (pyang@climate gsfc nasa gov).